University of Illinois at Urbana-Champaign

ACRC

Air Conditioning and Refrigeration Center A National Science Foundation/University Cooperative Research Center

Three-Dimensional Computational Modeling of Augmented Louver Geometries for Air-side Heat Transfer Enhancement

D. K. Tafti and J. Cui

ACRC TR-228 May 2004

For additional information:

Air Conditioning and Refrigeration Center
University of Illinois
Mechanical & Industrial Engineering Dept.
1206 West Green Street
Urbana, IL 61801

(217) 333-3115

Prepared as part of ACRC Project #114
Three-Dimensional Computational Modeling Of Augmented Louver Geometries for Air-side Heat Transfer Enhancement
D. K. Tafti, Principal Investigator

The Air Conditioning and Refrigeration Center was founded in 1988 with a grant from the estate of Richard W. Kritzer, the founder of Peerless of America Inc. A State of Illinois Technology Challenge Grant helped build the laboratory facilities. The ACRC receives continuing support from the Richard W. Kritzer Endowment and the National Science Foundation. The following organizations have also become sponsors of the Center.

Alcan Aluminum Corporation
Amana Refrigeration, Inc.
Arçelik A. S.
Behr GmbH and Co.
Carrier Corporation
Copeland Corporation
Daikin Industries, Ltd.
Delphi Thermal and Interior
Embraco S. A.
Fujitsu General Limited
General Motors Corporation
Hill PHOENIX
Honeywell, Inc.
Hydro Aluminum Adrian, Inc.
Ingersoll-Rand Company
Lennox International, Inc.
LG Electronics, Inc.
Modine Manufacturing Co.
Parker Hannifin Corporation
Peerless of America, Inc.
Samsung Electronics Co., Ltd.
Sanyo Electric Co., Ltd.
Tecumseh Products Company
Trane
Visteon Automotive Systems
Wieland-Werke, AG
Wolverine Tube, Inc.

For additional information:

Air Conditioning & Refrigeration Center
Mechanical & Industrial Engineering Dept.
University of Illinois
1206 West Green Street
Urbana, IL 61801

217 333 3115

Table of Contents

List of Figures

Page

Chapter 1. Three-Dimensional Flow and Heat Transfer Characteristics

Abstract

This study presents computational results in a complex three-dimensional louver geometry. The three-dimensionality occurs along the height of the fin, where the angled louver transitions to the flat landing and joins with the tube surface. The transition region is characterized by a swept leading edge and decreasing flow area between louvers. The results show that for Re_b = 1100, the flow on the angled louver is dominated by spanwise vortex shedding, which is weakly three-dimensional. On the other hand, the flow in the transition region exhibits strong three-dimensionality. A high-energy compact vortex jet forms in the vicinity of the louver junction with the flat landing and is drawn under the louver. The top surface experiences large velocities in the vicinity of the surface and exhibits high heat transfer coefficients. Although the flow slows down at the flat landing, the large induced velocities on the top surface increases the heat transfer coefficient on the tube surface.

Nomenclature

b	non-dimensional fin thickness (b^*/L_p^*)
f	non-dimensional characteristic frequency ($f^*L_p^*/u_\tau^*$)
F_p^*	dimensional fin pitch
F_p	non-dimensional fin pitch (F_p^*/L_p^*)
j	Colburn factor $j = \dfrac{Nu}{\mathrm{Re}_b \mathrm{Pr}^{0.4}}$
L_p^*	dimensional louver pitch (characteristic length scale)
Nu	Nusselt number, $Nu = \dfrac{L_p^* q''^* / (T_s^* - T_{ref}^*)}{\kappa}$
Pr	Prandtl number
q''^*	heat flux
Re_τ	Reynolds number ($u_\tau^* L_p^*/\nu$)
Re_b	Reynolds number ($u_b^* L_p^*/\nu$)
Re_{L_p}	Reynolds number $(V_c^* L_p^* / \nu)$
T_s^*	surface temperature
T_{ref}^*	reference temperature, integrated mixed mean
T	non-dimensional temperature, $T = T^* / (q''^* L_p^* / \kappa)$
t	non-dimensional time, $t = t^* u_\tau^*/L_p^*$
u_τ^*	friction velocity
u_b^*	bulk velocity
V_c^*	maximum bulk velocity based on nominal flow area in louver bank
x,y,z	non-dimensional coordinates, $x = x^*/L_p^*$, $y = y^*/L_p^*$, $z = z^*/L_p^*$

Greek symbols

α	thermal diffusivity
κ	thermal conductivity
ν	kinematic viscosity
θ	fluctuating non-dimensional temperature about the mean

Superscripts

* dimensional quantities

1. Introduction

Multilouvered fins are used extensively in the automobile and Heating, Ventilation and Air-Conditioning (HVAC) industries for enhancing air-side heat transfer in compact heat exchangers. They can be manufactured by high-speed production techniques and are more economical than other interrupted fin geometries. Researchers from universities and from the HVAC and automotive industries have published considerable amount of experimental visualizations and measurements, empirical correlations, and numerical simulations in this area. A review of past experimental and computational work can be found in Tafti et al. [1,2].

The heat transfer in multilouvered fins is influenced by three factors: a) duct versus louver directed flow [3,4]; b) thermal wake interference [5]; c) flow instabilities and transport of coherent vorticity in the vicinity of the louver surface [6]. These three phenomena can be captured with good precision in two-dimensional unsteady simulations. Factors (a) and (b) are primarily dependent on the two-dimensional geometrical parameters. The onset of unsteadiness is primarily a two-dimensional phenomenon, which can either be classified as a wake or Kelvin-Helmholtz instability [7], and can be resolved with accuracy in the initial stages of development. However, there is evidence [8,9,10], that as the Reynolds number increases beyond Re_{D_h} (based on hydraulic diameter) of about 2000-2500, secondary three-dimensional instabilities may be important. The intrinsic three-dimensionality, which develops in the flow field, cannot be resolved with two-dimensional simulations. It has the effect of reducing the coherence of the vortical structures, hence reducing their effectiveness in enhancing heat transfer.

Other than the intrinsic three-dimensionality that could develop at high Reynolds numbers, additional three-dimensionality is inherent in the multilouvered geometry near the junction of the louver with the tube surface, along the height of the fin in flat tube heat exchangers. The angled louver transitions to a flat landing, which extends to the tube surface as shown in Figure 1.1[1]. The extent of the transition region is estimated to be $0.5\,L_p^*$ [11]. A consequence of the manufacturing process is that the leading and trailing edges of the louver in the transition region, instead of being normal to the flow direction, exhibit a "sweep" angle to the flow direction. In addition to this effect, the open flow area between two subsequent louvers is restricted as the louvers approach the flat landing.

The objective of the present study is to perform high-resolution time-dependent simulations in the three-dimensional louver geometry by explicitly taking into account the transition region from louver to the tube surface, and to identify to what extent this junction affects the flow field and heat transfer, both locally and globally. In corrugated fins, the flow in this region is also important from the point of view of condensate management and carryover [12].

[1] In corrugated fins, the "flat landing" in not flat but curves at the junction with the tube. For current purposes we assume that the landing is flat.

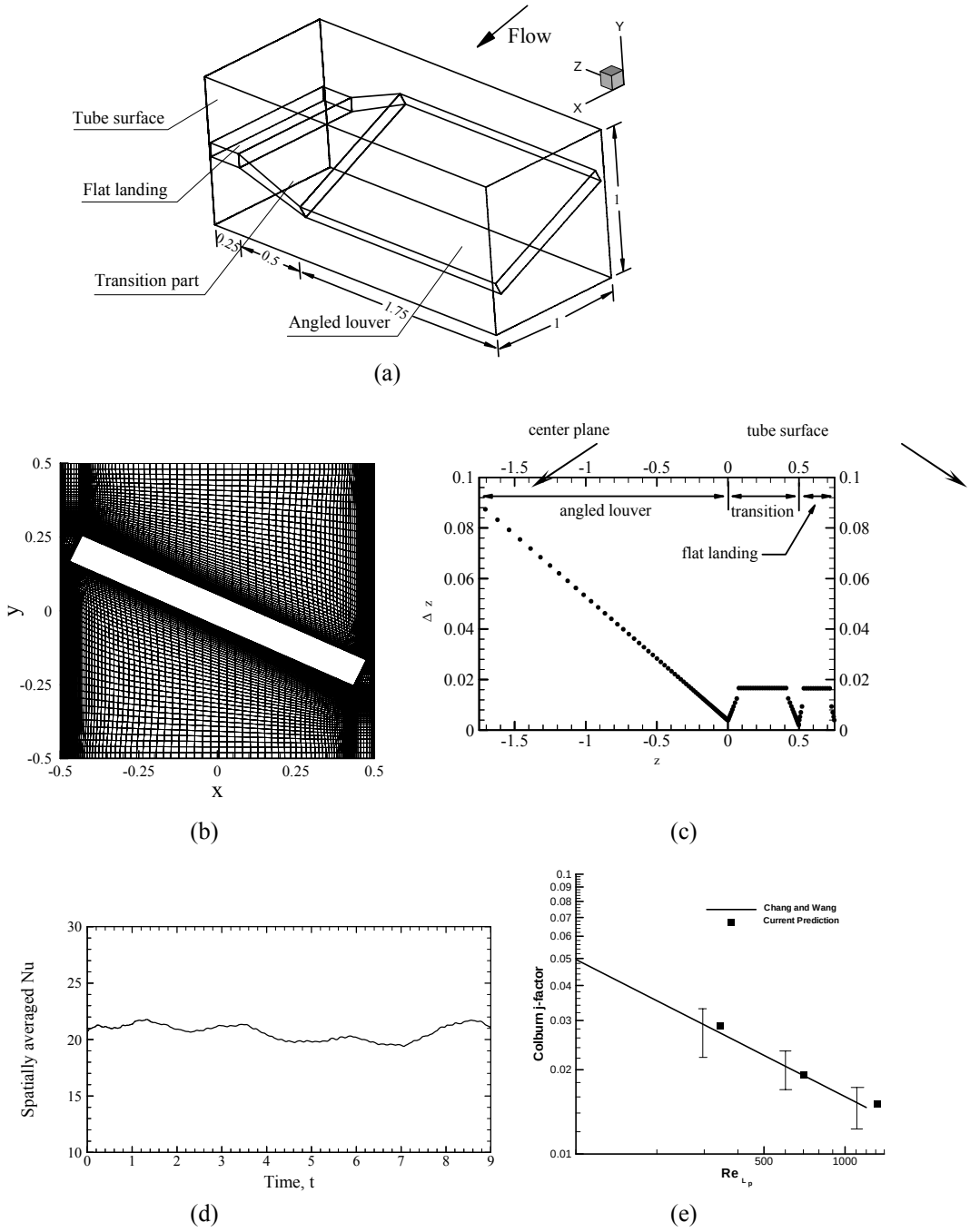

Figure 1.1. (a) Computational domain consisting of one louver representing an infinite array of louvers put together in the streamwise and cross-stream directions; (b) computational mesh in a *z*- plane; (c) grid distribution in the spanwise direction along the fin height, more grid points are distributed at the junction between the angled louver and transition region, and between transition region and flat landing; (d) Temporal evolution of the spatially averaged Nusselt number. The flow has adjusted to the mean pressure gradient and reached a statistically stationary state; (e) Comparison of calculated *j*-factors with CW correlation. $\mathrm{Re}_{L_p} = 1200$ corresponds to the calculation reported in this paper.

The paper is organized as follows: in the next section, a brief description of the numerical and computational method is given, followed by validation of the computational results. The results are presented by first introducing the unsteady dynamics of flow and heat transfer, followed by the mean time-averaged effects.

2. Numerical Formulation and Computational Details

The governing flow and energy equations are non-dimensionalized by a characteristic length scale, which in this case is taken to be the louver pitch, L_p^*, the friction velocity, $u_\tau^* = \sqrt{\Delta p_x^*/\rho}$ as the velocity scale, and $q''^* L_p^*/\kappa$ as the temperature scale. Here, Δp_x^* is the mean pressure gradient in the streamwise direction, q''^* is the specified dimensional constant heat flux on the louver and tube surface, and κ is the thermal conductivity of the fluid. The above non-dimensionalization results in a Reynolds number based on the friction velocity $Re_\tau = u_\tau^* L_p^*/\nu$, and Prandtl number $Pr = \nu/\alpha$, where ν and α are the kinematic viscosity and thermal diffusivity of the fluid, respectively.

For computational purposes, fully developed flow and thermal conditions are assumed in the multilouvered fins. The louvered fin geometry is approximated by an infinite array of louvers in both streamwise and cross-stream directions, which results in a simpler system with periodic repetition of the basic unit. The fully developed flow and heat transfer regime is experimentally observed to be attained by the second row in the streamwise direction for parallel-plate fins [13], and by the third or fourth row for louvered fins [14]. The unit computational domain for the base louver geometry has a dimension of 1 (normalized by louver pitch L_p^*) in streamwise (x) direction, fin pitch 1 (in this particular case, fin pitch F_p^* is same as L_p^*) in cross-stream (y) direction, and 2.5 in spanwise (z) direction, as shown in Figure 1.1(a). Along the spanwise direction, the louver can be divided into three parts: angled louver (length is 1.75), transition part (length is 0.5), and flat landing (length is 0.25). A linear transition profile is prescribed between the angled louver and the flat landing [15]. The thickness of the louver is 0.1 with 25° louver angle.

Periodic boundary conditions for velocity, modified pressure and temperature are applied in the streamwise and cross-stream directions since the flow is assumed to be both hydrodynamically and thermally fully developed without any entrance or exit effects. The application of periodic boundary conditions in the streamwise direction requires that pressure and temperature be re-formulated as in Patankar et al. [16]. No-slip, no-penetration boundary conditions for velocity and constant heat flux conditions are enforced on the louver surface and the tube surface. Along the fin height at a distance of 2.5 from the tube wall, it is assumed that the flow is sufficiently removed from the extrinsic three-dimensional effects of the transition region and is nominally two-dimensional. This facilitates the application of symmetry boundary conditions. Our results show that this assumption is well justified.

The governing equations for momentum and energy are discretized with a conservative finite volume formulation using a second-order central difference scheme. A non-staggered grid topology is adopted. The Cartesian velocities, pressure, and temperature are calculated and stored at the cell center, whereas contravariant fluxed are stored and calculated at the cell faces. For the time integration of the discretized continuity and

momentum equations, a projection method is used [17]. The temporal advancement is performed in two steps, a predictor step, which calculates an intermediate velocity field, and a corrector step, which calculates the updated velocity at the new time step by satisfying discrete continuity. The energy equation is advanced in time by the predictor step.

The computational mesh consists of 98 zones in ξ - and η - directions, respectively, and 128 zones in ζ - direction along the fin height. The grid is clustered in the vicinity of the louver, in the transition zone and tube wall region for better resolution. The mesh is partitioned into sixteen blocks in the spanwise direction. Each block (98×98×8) is assigned to a processor in a distributed programming environment. The calculations are performed on 16 processors of SGI-Cray Origin 2000. The Reynolds number, Re_τ, is 400, which gives a bulk Reynolds number Re_b, based on the calculated bulk velocity and louver pitch, of approximately 1100. This lies at the high end in typical applications. The time step used in the computation is 5×10^{-5}. Initial conditions are obtained from an analogous two-dimensional simulation over the angled louver. The two–dimensional solution is duplicated in the spanwise direction along the height of the fin. Since the flow rate adjusts to the imposed pressure gradient, it is much more economical to run a separate two-dimensional simulation, which gives a fairly good estimate of the bulk flow velocity to begin with, than to simulate the same transient process in the three-dimensional calculations.

The flow at this Reynolds number is also time-dependent. Hence the flow not only has to adjust to the mean pressure gradient but also reach a statistically stationary state. Time series data of field variables are carefully monitored and stationarity is claimed when these data show a near constant mean value or a quasi-periodic fluctuation in time. Figure 1.1(d) shows the stationary time evolution of the spatially averaged Nusselt number calculated on the louver surface for the last 9 time units of the simulation. Stationarity is well established with a mean value around 22.7 with a maximum fluctuation within 5% of the mean value. Unless otherwise noted, all mean quantities are obtained by averaging over the last three non-dimensional time units (from time t = 6-9).

To characterize the heat transfer, we define a local instantaneous Nusselt number. The surface-averaged Nusselt number is obtained by integration over the louver surface. In this paper, reference to the surface-averaged Nusselt number refers to the entire louver surface (excluding tube surface), whereas locally surface-averaged Nusselt number refers to the average Nusselt number in each computational block.

More details of the numerical algorithm, treatment of the boundary conditions, verification of the computer program and domain decomposition for parallel computing can be found in Tafti et al. [1,2].

3. Validation of Numerical Results

Numerical accuracy and resolution are crucial issues in time-dependent calculations in complex geometries. More often than not, quantitative validation of the calculation is challenging because of the lack of detailed three-dimensional experimental data, the expense and inability to perform grid independency studies, and by the lack of *a-priori* knowledge of the flow field. The three-dimensional louver geometry has the potential for generating highly complex and three-dimensional flow and thermal fields. Hence, *a-priori*, the grid must be designed intelligently such that energetic eddies are appropriately resolved. To do this we have drawn on our experience with two-dimensional unsteady simulations [6], where we have established through grid refinement studies, that a mesh resolution of 96×96 computational cells in the z- plane surrounding a louver is sufficiently fine to capture all the

important dynamics of flow oscillations. Figure 1.1(b) shows the computational mesh in a z- plane in the angled louver portion. The grid is clustered in the vicinity of the louver with the first grid point above the louver surface at 0.0019 (in non-dimensional unit), which falls between 0.1 and 0.3 in local wall units[2] based on the local shear stress. In the region with the highest shear stress (in the transition region), there are five grid points within 10 wall units normal to the surface, with the first one at 0.3. Attention has also been given to the grid distribution in the streamwise and spanwise directions. Along the streamwise direction, the grid is nearly uniform with spacing of 5-7 wall units. Along the fin height or spanwise direction, the mesh distribution is clustered in the transition region and the tube surface. Figure 1.1(c) shows the spanwise grid distribution Δz versus z. The mesh is coarsest in the two-dimensional region of the geometry with the maximum spacing of 60 wall units and finest at the beginning and end of transition, and near the tube wall with the spacing around 3 wall units. This gives us confidence that the boundary layers on the louver and tube surface are very well resolved. Since most of the energy is adequately resolved, there is no need to use any subgrid-scale stress models.

Another validation is to check the force balance on the louver. In the current simulation, a mean pressure gradient is imposed in the streamwise direction to drive the flow. Consequently, this pressure force should be balanced by the sum of the form (pressure) drag force and friction drag force from the louver surface and the friction drag force from the tube surface. The form drag acting on the louver surface is nearly three times the friction drag, which is fairly typical of louver geometries. The force balance between the imposed force and the forces from the louver and tube surface is verified (with an error at 0.6%). This validates the numerical formulation and the adequacy of the time averaging sample size.

Finally we compare the calculated overall Colburn j-factor (louver + tube) with the correlation of Chang and Wang [18] (CW). This is a general correlation developed from experimental data available for different types of louver geometries. The following geometrical values are used in the correlation (all lengths are normalized by louver pitch): $F_p = 1$, $\theta = 25$ degrees, $b = 0.1$, fin height = tube pitch = 5, tube depth = 15, and louver length = 4.5[3]. Figure 1.1(e) plots the j- factor for three calculated Reynolds numbers, from which the largest corresponds to the calculation reported in this paper. Also plotted are upper and lower bounds of the experimental data from which the CW correlation was derived. The calculated j-factors are well within experimental scatter, and in fact compare quite well with the correlation.

4. Results

The imposed pressure gradient of unity and $Re_\tau = 400$, give a calculated bulk Reynolds number Re_b of approximately 1100. In general the flow is unsteady with self-sustained flow oscillations. The flow oscillations manifest themselves as spanwise vortices, which are nominally two-dimensional in nature with weak three-dimensionality across the fin height. In the transition region, the flow exhibits strong three-dimensionality with

[2] This is calculated *a-posteriori* by extracting the time mean wall shear stress from the calculation. For reference, a fully turbulent channel flow calculation is adequately resolved by the current procedure with 5 grid points within 10 wall units normal to the wall, and a resolution of approximately 30 and 10 wall units in the streamwise and spanwise directions, respectively.

[3] Tube depth is used in the same context as flow depth. In our calculations, the flow depth is infinity. So a typical value of 15 is used.

additional unsteady phenomena. For the most part, the flow encountered at this Reynolds number, lie in the unsteady laminar to chaotic regimes.

First, the unsteady phenomenon governing flow and heat transfer are discussed and then their effect on the mean flow and thermal fields is presented.

4.1. Coherent Vorticity Dynamics

To characterize the unsteady nature of the flow and the associated vorticity dynamics, the $\nabla \boldsymbol{u}$ [19] vortex identification technique is used. The method has been used by a number of researchers in extracting coherent vorticity [10,20]. This frame-invariant method identifies vortical structures as regions of large vorticity, where rotation dominates over strain to cause the rate-of-deformation tensor $\nabla \boldsymbol{u}$ (velocity gradient tensor) to have complex eigenvalues (one real and two conjugate complex eigenvalues). The complex eigenvalues imply that the local streamline pattern is closed or spiral, thus correctly eliminating near-wall shear layers. This methodology can also be separately applied in the x-, y-, or z- planes in order to identify streamwise, cross-flow, and spanwise vortices [10], respectively. The strength of the vortex is measured in terms of the imaginary part of the eigenvalue of the velocity gradient tensor and is denoted by λ_i. The strength of its three subsets, streamwise, cross-flow, and spanwise vortices is measured in terms of the imaginary part of the eigenvalue of the velocity gradient on the x-, y-, and z- planes, respectively, and is denoted by $\lambda_{i,x}$, $\lambda_{i,y}$, and $\lambda_{i,z}$, respectively.

Figure 1.2 displays the temporal evolution of spanwise vortices represented by $\lambda_{i,z}$ contours in the z- plane at the angled part of the louver at z = -1.46. For presentation purpose, the vortices are labeled by letters, and a "+" sign implies vortices shed from the bottom surface of the leading edge and a "–" sign implies those shed from the top louver surface. The numbers denote the magnitude of $\lambda_{i,z}$ at the vortex center. At time t = 0.00, Figure 1.2(a), vortex shedding from both top and bottom surface at the leading edge is clearly evident, in spite of the flow not being completely aligned with the louver. Near the leading edge, vortex A^- and I^+ have the same strength and I^+ is about to shed another vortex. However, comparison of the strength of vortices shed from the top and bottom surface (vortex B^- and J^+, vortex C^- and K^+) show significant differences. The vortices shed from the top surface are a factor of 2-3 stronger than those shed from the bottom edge[4]. We also see strong interactions between leading and trailing edge vortices. The trace of vortex K^+ in Figure 1.2(a-c), J^+ in Figure 1.2(d-f), and C^- in Figure 1.2(b-e), suggests that vortices shed from the leading edge shear layer, merge with vortices at the trailing edge and pick up strength before convecting into the wake.

[4] The vortices shed from the leading edge of the bottom surface are weak and are difficult to sense without isolating them from the background vorticity.

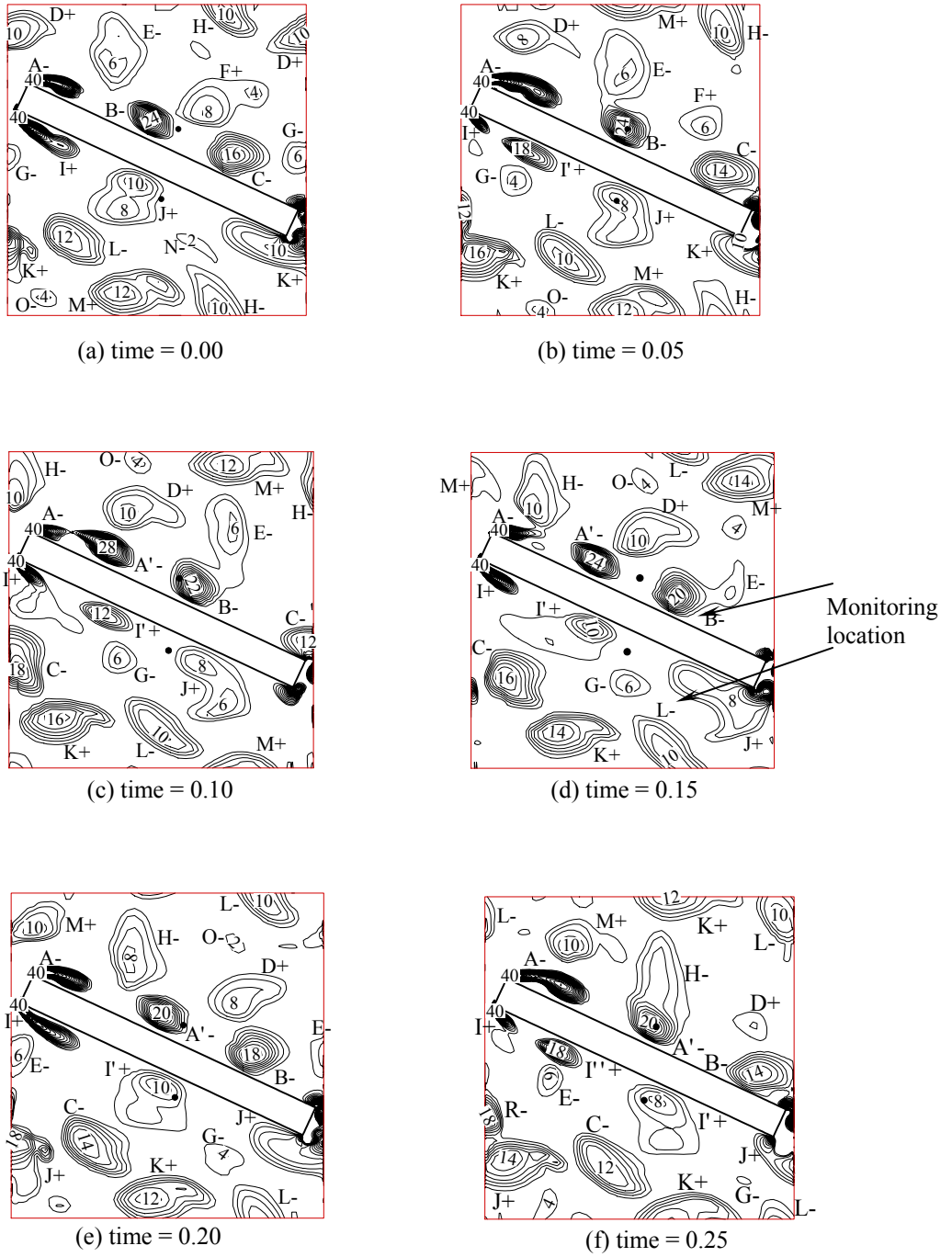

Figure 1.2. Temporal evolution of coherent spanwise vortices represented by $\lambda_{i,z}$ contours in the z-plane at z = -1.46. Contour levels are in steps of 2 ranging from 0 to 40. Vortices shed from the leading edge, combine with wake vortices and also interact with upstream shed vortices.

Because of the periodicity, vortices leaving the domain, re-enter the domain again (see vortex D^+, H^-, G^- and K^+). The corresponding spatial interpretation of vortex trajectories shed from a louver is shown in Figure 1.3(a). In the snapshot at t = 0.0, the immediate wake of the louver is represented by the alternating vortices (K^+, L^-, M^+, H^-

), which convect further downstream to become (D^+, E^-, F^+, G^-). The vortices have a spatial life span of approximately 3 to 4 louvers pitches from the time they are generated at the leading edge.

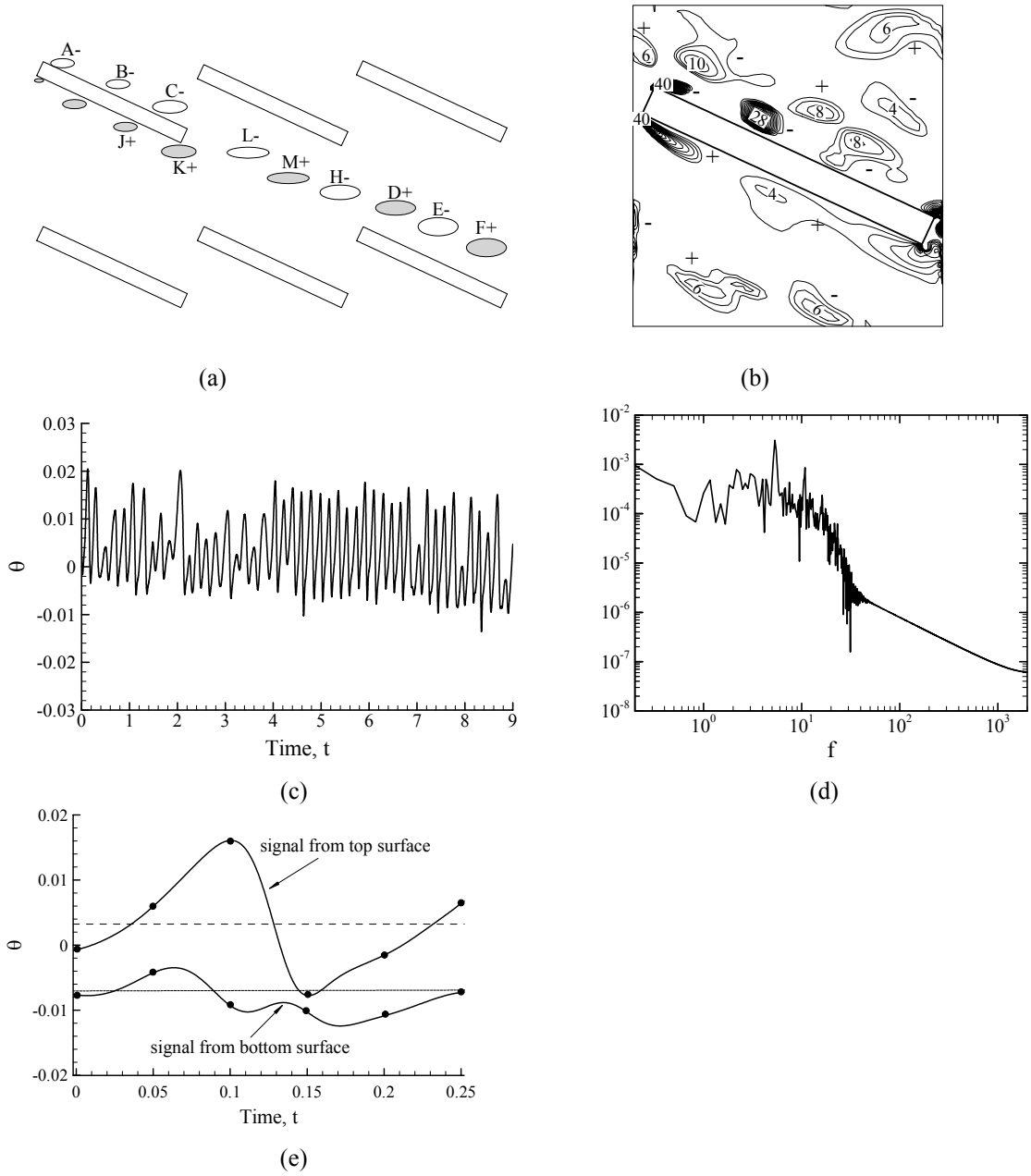

Figure 1.3. (a) Trajectory of vortices shed from a single louver as derived from Figure 1.2; (b) contours of $\lambda_{i,z}$ at time t = 0.00 in the z- plane at z = -0.122, just before the start of the transition region. Vortices are diffuse and weaker than at z = -1.46; (c) temperature signal and (d) frequency spectrum at plane z = -1.46 in the angled louver portion. The monitoring location is near the middle of louver and is 0.065 in normal distance from the louver top surface; (e) temporal evolution of temperature on the top and bottom surface of the louver corresponding to the vortex shedding cycle shown in Figure 1.2.

Vortex-vortex interactions are also observed on the top surface of the louver. At time t = 0.05, Figure 1.2(b), vortex I'^+ is shed from the shear layer on the bottom surface. Vortex B^- begins to interact with vortex E^- (from

the wake of a previous louver) as both move downstream. As they approach the trailing edge, at $t = 0.20$ in Figure 1.2(e) they separate again. Similar interactions can also be observed in Figure 1.2(f) between $A^{'-}$ and H^{-}. We also take note of the fact that a vortex is always shed from a leading edge shear layer in the presence of a vortex of opposite sign from the wake of a previous louver. For instance, vortex $A^{'-}$ is shed in the presence of D^{+}, whereas $I^{'+}$ is shed in the presence of G^{-}.

The vorticity dynamics observed in Figure 1.2 is present throughout the angled portion of the louver, which is dominated by the periodic shedding of spanwise vorticity. Figure 1.3(b) plots contours of $\lambda_{i,z}$ in the z- plane at $z = -0.122$, just before the louver starts its transition, at one instant in time, $t = 0.00$. The vortices are much more diffuse and weaker in this region. However, in spite of this there is a good correlation with Figure 1.2(a), and the flow is still preferentially two-dimensional with weak three-dimensional effects.

Figure 1.3(c-d) shows the time history and corresponding frequency spectrum, respectively, of the temperature signal at the angled louver close to the plane of symmetry. The monitoring location is above the top louver surface and at the middle of the louver. The time signals exhibits a nearly periodic pattern, which is consistent with the periodic vortex shedding from the leading edge on the louver top surface observed from the flow animations. The frequency spectrum shows a clear peak at $f \approx 5.2$, which corresponds to the frequency of vortex shedding observed in Figure 1.2. Based on louver pitch and the bulk velocity, the characteristic non-dimensional frequency is 1.87. This value compares well with the value of 2 obtained in previous two-dimensional calculations [6] of developing flow and heat transfer in multilouvered fins.

There is considerable evidence in Figure 1.2 that vortex shedding from a louver does not proceed in isolation but is influenced by other louvers as well, until a characteristic "louver bank" frequency is established. This agrees with the experiments of Mochizuki and Yagi [21] and also our two-dimensional numerical studies [6]. Mochizuki and Yagi [21] in their experiments with staggered fin arrangements, found that multiple frequencies were observed for arrays which were less than 8 columns deep, however, once the depth of the array increased beyond this point, single characteristic frequencies were found, thus indicating that vortex shedding in large arrays was influenced by factors other than individual plates. Tafti and Zhang [6], in two-dimensional developing flow in multilouvers also reached similar conclusions. They found that the characteristic frequencies did not scale with louver thickness, as it would in the case of isolated plates, but scaled with a length scale associated with the fin pitch, and postulated from this that the interaction of convecting vortices played a major role in fixing the characteristic frequency.

The flow takes on added complexity in the transition region. It is strongly three-dimensional and the flow dynamics are quite different. To illustrate this, Figure 1.4(a) plots the distribution of volume averaged $\lambda_{i,x,y,z}$ as a function of fin height at an arbitrary instant in time. Only the volumes with non-zero eigenvalues are included in the volume averaging. On the angled louver, λ_i essentially maintains a constant value, with a dominant contribution from spanwise vorticity. However, in the transition region, λ_i increases, with increasing contributions from streamwise and cross-stream vorticity, with a drop in contributions from spanwise vortices. λ_i reaches a maximum in the center of the transition region and then decreases as the louver approaches the flat landing and the tube surface.

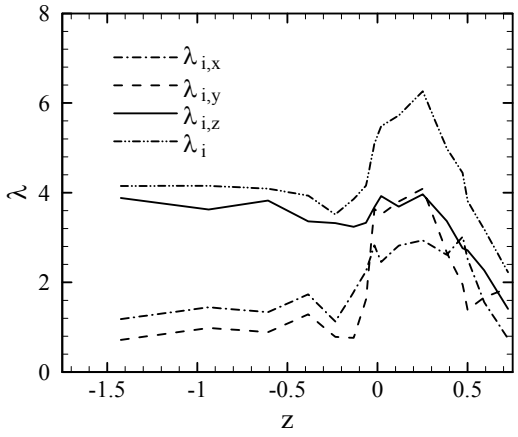

(a)

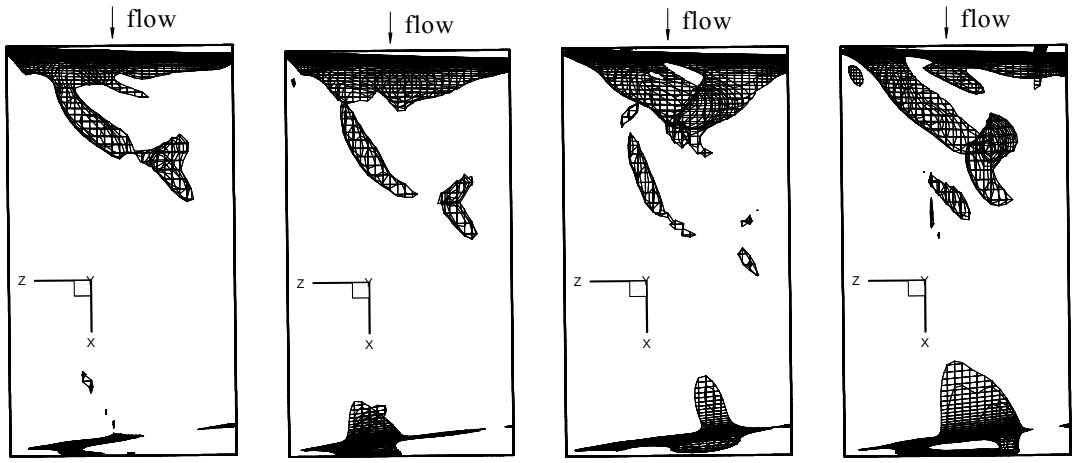

time $t = 0.00$ $t = 0.05$ $t = 0.10$ $t = 0.15$

(b)

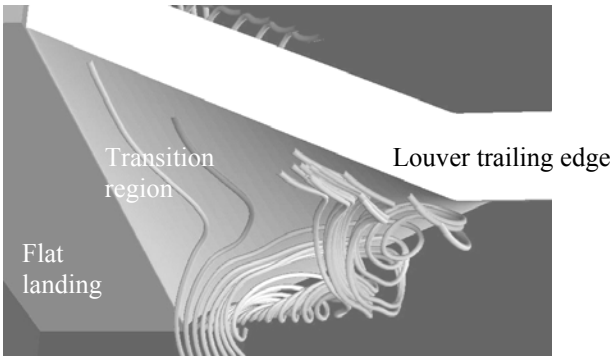

(c)

Figure 1.4. (a) Volume-averaged vortical strength distribution along the fin height at an arbitrary instant; (b) surface contours of $\lambda_i = 30$ at the bottom of the louver in the transition region. There is periodic formation and detachment of vorticity from the leading edge region; (c) instantaneous streamtubes injected near the leading edge of the louver near the junction with the flat landing, seen from louver bottom.

Figure 1.4(b) plots the surface contours of $\lambda_i = 30$ at the bottom of the louver in the transition region. This includes all components of coherent vorticity. An agglomeration of coherent vorticity is found at the leading edge of

the louver at all time instances. This is mostly spanwise vorticity which is formed by the interaction of the flow with the leading edge. The elongated zone of vorticity near the junction with the flat landing mostly consists of contributions from streamwise and cross-stream vorticity and is the coherent core of a "vortex jet" which forms in this region. The decreasing flow area between two adjacent louvers, adds considerable translational energy to the flow between louvers. Part of the flow accelerates over the top surface, while the remaining part is drawn underneath the louver. The sweep angle of the leading edge in turn adds rotational energy to the flow which is drawn underneath the louver. This results in a region of concentrated streamwise vorticity, which forms the core of the vortex jet. In general the vortex jet follows a trajectory away from the tube surface and towards the angled louver. It also moves away from the louver surface. We also observe that the core, which is made up of the elongated zone of vorticity, periodically forms and detaches from the leading edge on a time scale of about $t = 0.2$.

Figure 1.4(c) plots a snapshot of instantaneous stream tubes injected in the leading edge region of the louver. A region of intense rotation can be identified near the leading edge. In spite of the small spatial extent of the core, the intense rotational energy entrains fluid from the surroundings — it grows and quickly loses its coherency within half a louver length.

Figure 1.5(a-d) plots the time signals of temperature, and the respective spectra at two locations in the transition region. One location is in the middle of the transition region at $z = 0.243$ and the other nearer the flat landing at $z = 0.424$, both on the top surface of the louver. The signals are more chaotic and exhibit a higher energy content than their counterparts in the vicinity of the angled louver. There is no clear indication of a characteristic frequency as in Figure 1.3. However, at both locations there is considerable low frequency energy in the signal. The strong low frequency content is quite pronounced in Figure 1.5(c-d) at the location near the flat landing, at a frequency of approximately 0.3. This is also present in Figure 1.5(a-b), but is not as well defined. Similar observations are made at the bottom of the louver, for both temperature and velocity fluctuations. The discussion on the cause of the low frequency oscillation and its dynamics and effect on heat transfer is deferred to the next section.

In summary, the periodic shedding of spanwise vortices dominates the flow field on the angled part of the louver. Because the flow is nearly aligned with the louver direction, vortices are shed from both the top and bottom leading edges, however, the vortices shed from the top are 2-3 times stronger. There is considerable interaction between vorticity shed from the leading and trailing edge of louvers, and also between louvers. The dynamics of vortex shedding in this region is nominally two-dimensional. In the transition region, the flow is strongly three-dimensional. It is dominated by an unsteady vortex jet, which flows underneath the louver, and strong flow acceleration. The region is characterized by nearly equal contributions from all three components of coherent vorticity, with a net increase in overall magnitude. Time signals and spectral plots indicate a quasi-periodic low frequency oscillation in this region.

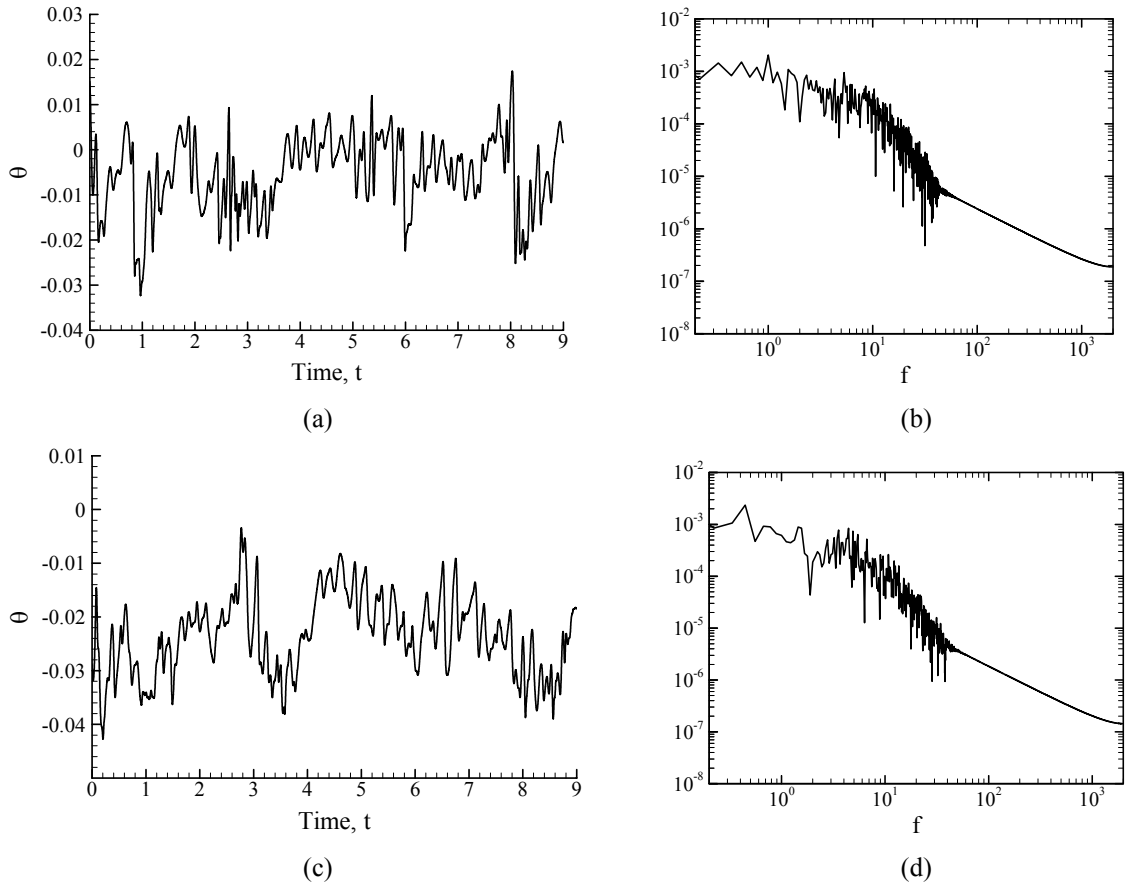

Figure 1.5. Signal analysis at plane $z = 0.243$ near the middle of the transition region (a) temperature signal (b) temperature frequency spectrum. The monitoring location is near the middle of louver and is 0.060 in normal distance from the louver top surface; similar signal analysis at plane $z = 0.424$ near the flat landing; (c) temperature signal (d) temperature frequency spectrum. The monitoring location is near the middle of louver and is 0.052 in normal distance from the louver top surface.

4.2. Unsteady Heat Transfer Characteristics

Here we evaluate the effect of the unsteady flow field on the instantaneous heat transfer on the louver surface. On the angled louver, the heat transfer is dominated by the impinging flow on the bottom of the louver surface and the spanwise vortices on the top surface. It has been established in previous studies [10] that spanwise vortices act as large-scale mixers. The augmentation in heat transfer depends on the strength of the vortex and its location with respect to the surface [10]. Vortices embedded at the edge of the boundary layer, through their rotational energy bring in free-stream fluid in the vicinity of the heat transfer surface. The induced fluid mass then picks up heat from the surface and is ejected back into the free-stream. Figure 1.3(e) plots the temporal evolution of temperature on the top and bottom surface of the louver corresponding to the vortex shedding cycle shown in Figure 1.2. The measurement locations are located at $z = -1.46$ near the middle of the louver and are shown in Figure 1.2. The temperature variation with time corresponds to the passing of vortex B^- and then $A^{'-}$ on the top surface and vortex J^+ and $I^{'+}$ on the bottom surface. On the downstream side of the vortex, free-stream fluid is induced towards the louver, resulting in the low temperature valley at $t = 0.15$ corresponding to vortex $A^{'-}$. As the vortex convects downstream of the measurement location a peak in temperature results as the heat carrying fluid is ejected out back

into the free-stream. This occurs at $t = 0.10$ after the passage of vortex B^-. The passage of vortices on the bottom surface do not have a large effect on heat transfer.

Figure 1.6 plots the temporal evolution of local surface averaged Nusselt numbers from $z = 0.25$ to 0.5 in the transition region near the flat landing. Both, the top and bottom surface of the louver show large quasi-periodic variations in Nusselt number at intervals of approximately 2 to 3 non-dimensional time units. The Nusselt number on the top surface is characterized by short bursts of intense activity in the region near the flat landing, with relatively long periods of calm. Activity is more frequent and less intense on the louver bottom surface. The events which lead to the fluctuations in Nusselt number occur around the same time on both the top and bottom surface indicating that the two are correlated.

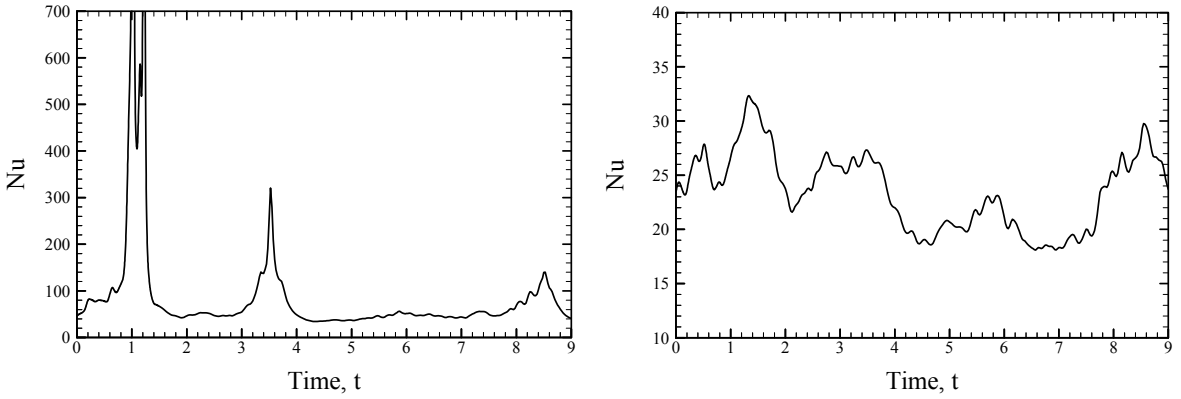

(a) on top louver surface (b) on bottom louver surface

Figure 1.6. Temporal evolution of surface averaged Nusselt numbers from $z = 0.25$ to 0.5 in the transition region near the flat landing. The low frequency events on the top and bottom surface are correlated.

To understand what causes the large increase in the local Nusselt number on the top surface, Figure 1.7(a-d) plots the instantaneous velocity vectors and temperature contours on the top surface in a z- plane ($z = 0.424$) near the flat landing. The vectors are plotted at three locations along the length of the louver. At $t = 3.5$, when the Nusselt number on the top surface is high, the flow velocity in the vicinity of the louver is very high, which significantly reduces the thickness of the thermal boundary layer and leads to very high heat transfer. The resulting effect on the temperature of the louver surface is shown in Figure 1.7(b). A low temperature zone exists (high heat transfer) in the region near the flat landing, which extends throughout the length of the louver. Whereas at $t = 4.5$, the flow velocity is not as energetic and subsequently its effect on louver heat transfer is not quite that strong. We note that even in its non-energetic state, the high velocities near the top surface provide enhanced heat transfer compared to the angled portion of the louver.

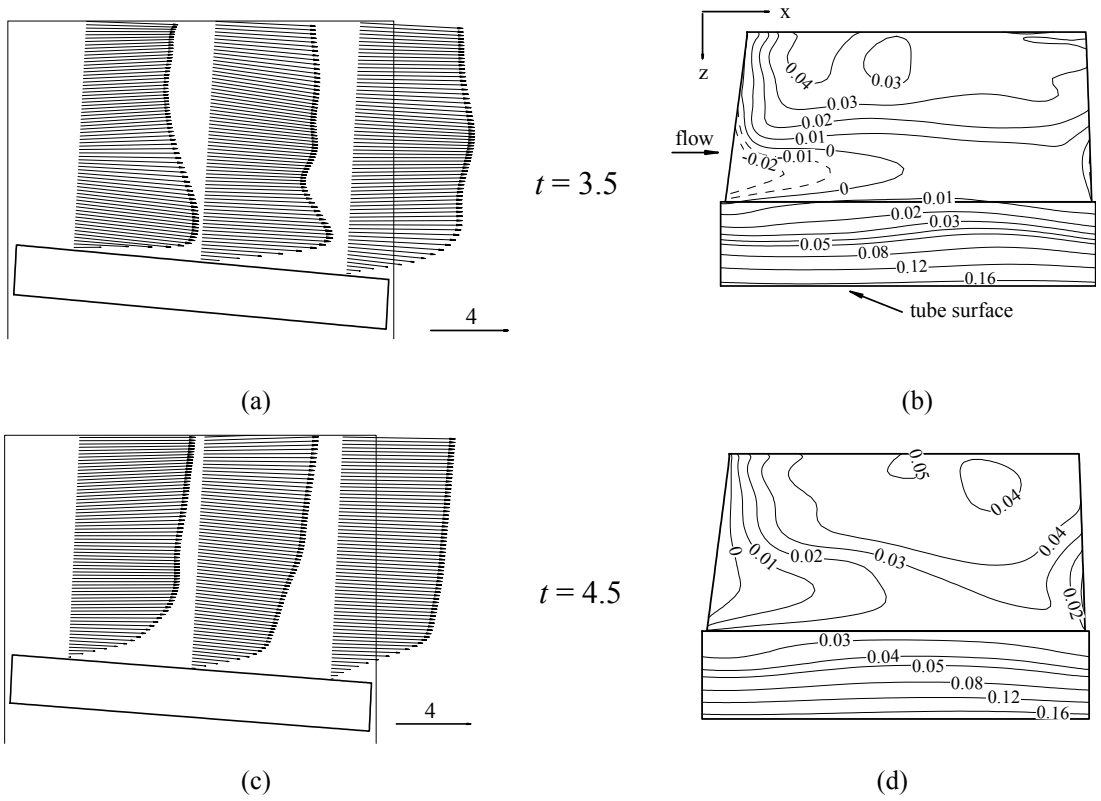

Figure 1.7. (a) Instantaneous velocity vectors and (b) temperature contours on the top surface in a z- plane at z = 0.424 in the transition region near the flat landing at time t = 3.5; (c) instantaneous velocity vectors and (d) temperature contours at the same location at time t = 4.5. The accelerating flow on the top surface increases heat transfer. Arrow shows scaling of vectors.

The dynamics of Nusselt number fluctuations on the bottom surface is related to the dynamics of the vortex jet and its effect on the flow. Figure 1.8(a-f) plots instantaneous surface contours of $\lambda_i = 30$ in the transition region at t = 1.5 and t = 4.5, corresponding to a peak and valley, respectively, in Figure 1.6. At t = 4.5, the vortex jet is dominant in the leading edge region and its proximity to the surface induces a recirculation zone underneath it in the leading edge region. Hence during this state the jet has a detrimental effect on heat transfer which can be surmised from Figure 1.8(f). A region of high surface temperature and low heat transfer correlates roughly with the location of the vortex jet. On the other hand at t = 1.5, the vortex jet has detached from the leading edge region and the core that remains attached has a different spatial location and orientation. Again, we find that the instantaneous temperature contours on the surface correlate with the location of the jet. However, unlike at t = 4.5, the temperatures are much lower, not only in the vicinity and underneath the jet but also in the vicinity of the trailing edge of the louver. The substantially lower temperatures near the trailing edge is due to increased flow velocity, which is caused by the formative vortex jet at the leading edge of the louver downstream.

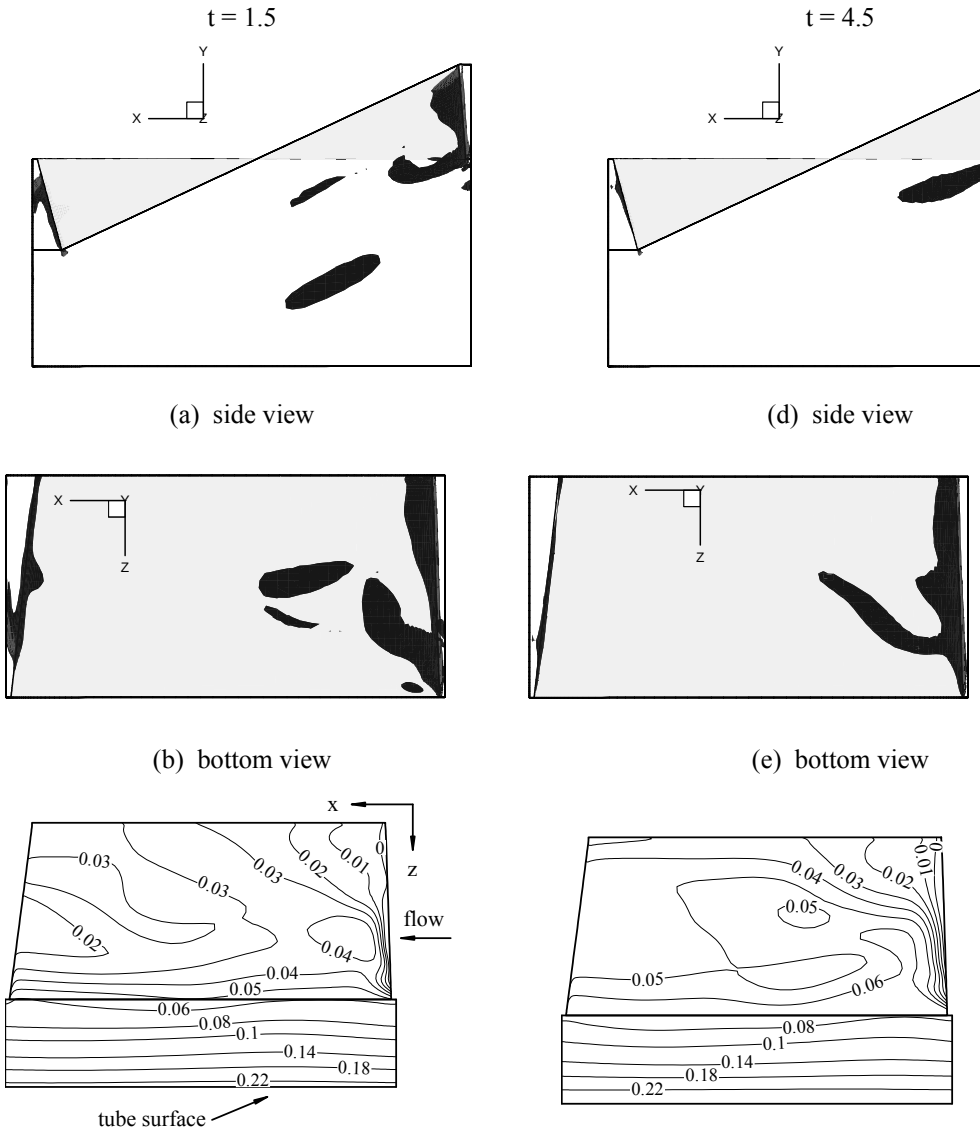

Figure 1.8. (a) Side view and (b) bottom view of instantaneous surface contours of $\lambda_i = 30$ in the transition region, and (c) the temperature contours on the louver bottom surface at time $t = 1.5$; (d) side view and (e) bottom view of the instantaneous surface contour of $\lambda_i = 30$ in the transition region, and (f) the temperature contours on the louver bottom surface at time $t = 4.5$. The heat transfer on the bottom surface is closely related to the dynamics of the vortex jet.

We postulate a scenario in which the dynamics of the vortex jet underneath the louver affects the movement of fluid on the top surface of the louver or vice versa. The location, state, and strength of the vortex jet affects the trajectory of fluid on the top surface. From the evidence we have seen, it seems that a strong attached vortex jet at the bottom pushes the high velocity fluid on the top surface away from the louver surface and limits the heat transfer augmentation. When the vortex jet destabilizes, detaches and starts forming again, high velocity fluid on the top surface is drawn to the vicinity of the louver surface which results in high heat transfer. At the same time, the detached jet and its subsequent formation also increases heat transfer on the bottom surface. In addition to this

occurring on a long time scale (t = 2-3), the jet also destabilizes and forms on a much shorter time scale of t = 0.2-0.3, as seen in Figure 1.4. Correspondingly, the extent of the high velocity region in the vicinity of the top louver surface also oscillates. This can be clearly discerned from flow animations. However, the fast time scale variations are not as strong and sustained as the long time scale variations.

4.3. Mean Flow and Heat Transfer

Figure 1.9(a-d) shows the time mean velocity vectors at four z- planes. At the angled louver part (Figure 1.9(a)), the vectors are quite parallel to the louver surface, indicating the flow is essentially louver-directed at this Reynolds number and louver angle. Near the leading edge on the louver top surface, a mean recirculation zone can be identified which is a result of the separated shear layer at the leading edge. Away from the surface, the flow recovers quickly and a velocity overshoot represents the separated shear layer. At the middle of the louver, flow reattaches to the louver surface and a boundary layer starts to develop. The boundary layer grows as the flow moves downstream toward the trailing edge. At this location, the vectors far away from the louver surface show a downward motion as the flow approaches the leading edge of the downstream louver. On the louver bottom, the flow remains attached and the boundary layer grows as the flow proceeds downstream. The wake of the upstream louver is visible at the first two locations and recovers gradually as the flow moves further downstream

In the transition region, the flow field is quite different (Figure 1.9(b)). This z- plane is at the middle of the transition zone and the louver angle has decreased from 25° in the angled louver part to 10.4°. Although not represented in Figure 1.9(b), the flow is three-dimensional with substantial momentum transport occurring along the fin height or spanwise direction. On the top surface, near the leading edge and at the louver middle, the velocity distribution appears to be nearly uniform with large defects in the vicinity of the louver. At the last station, the velocity profile has recovered, most likely from spanwise and cross-stream momentum transfer, as the flow near the louver is drawn down into its wake. On the other hand, flow away from the louver surface flows over the leading edge of the downstream louver. The first profile on the bottom of the louver captures the initial core of the vortex jet before it moves out of the plane. As explained in the previous section, the jet forms as a consequence of the translational and rotational energy imparted to the fluid in this region. The strong shear layer of the jet produces a recirculation zone underneath it on the louver surface.

Figure 1.9(c) shows similar profiles at a location near the flat landing at z = 0.424. Large fluid velocities are evident on the top surface of the louver particular in the region immediately following the leading edge. This plane is in the region where the shear stress reaches a maximum and the velocity profiles are closest to that in a turbulent flow over a flat plate. In this region, the flow area between louvers narrows considerably. Hence flow from the top surface of the louver is not drawn underneath in its wake. Consequently, it impinges on the leading edge of the following louver and accelerates over the top surface. The flow at the bottom of the louver also moves in the streamwise direction at the trailing edge and impinges on the bottom surface of the downstream louver as seen in Figure 1.9(c).

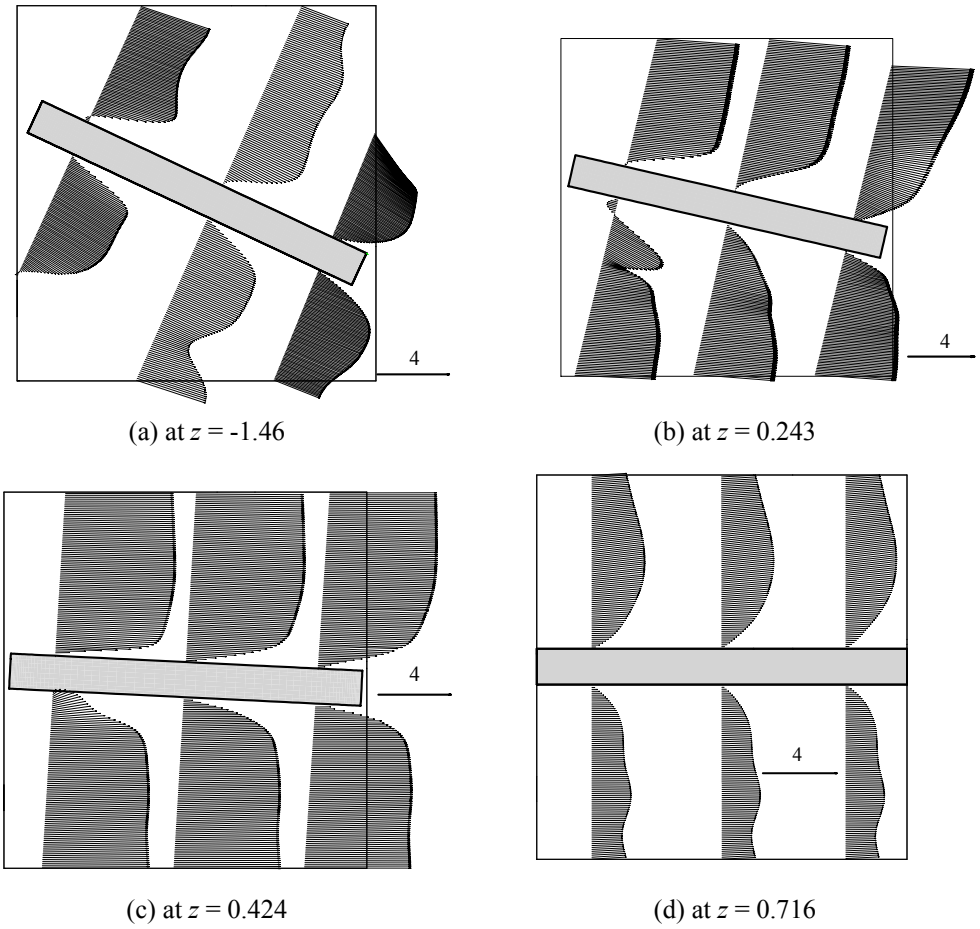

(a) at z = -1.46 (b) at z = 0.243

(c) at z = 0.424 (d) at z = 0.716

Figure 1.9. Time mean velocity vectors at four z- planes, (a) on the angled louver; (b) at the middle of the transition region; (c) near the flat landing; (d) on the flat landing. The acceleration in the transition region is clear. Arrow shows scaling of vectors.

On the flat landing (Figure 1.9(d)), as we approach the tube surface at z = 0.716, the velocity decreases considerably as it is engulfed in the boundary layer on the tube surface. However, we find that the velocity in the vicinity of the top surface is higher than at the louver bottom. This is due to the residual effect of the strong flow velocities in its vicinity. Although, the profiles imply that the flow is laminar and steady, flow animations show that the boundary layer on the tube surface, although laminar, is not steady and undulates on a long spatial and temporal wavelength in response to the flow dynamics adjacent to it in the transition region.

Figure 1.10(a-d) shows thermal fields at the angled louver portion, transition zone, and flat landing. One of the consequences of the louver flattening out is that the thermal wake of the louver starts interfering with the bottom surface of the louver immediately downstream of it. Hence in this region, the combination of the thermal wake effect and the recirculation zone induced by the vortex jet reduces the heat transfer coefficient on the lower surface of the louver. On the other hand, the high velocity on the top surface and its close proximity to the louver surface increases the heat transfer coefficient. This can be surmised by the relatively thin thermal boundary layer on the top surface in the transition region. In the angled part of the louver, the thermal boundary layer on the top surface is thicker than that on the bottom surface of the louver. Generally, the effect of the large-scale vortices is to shorten

the mean recirculation region and enhance heat transfer downstream of it. On the bottom surface, because the oncoming flow impinges near the leading edge, the thermal boundary layer is thinnest in this region and increases downstream. At the flat landing, temperatures are much higher since the flow is engulfed in the louver as well as the tube thermal boundary layer. However, we find that the thermal boundary layer on the top surface is much thinner than that on the lower surface.

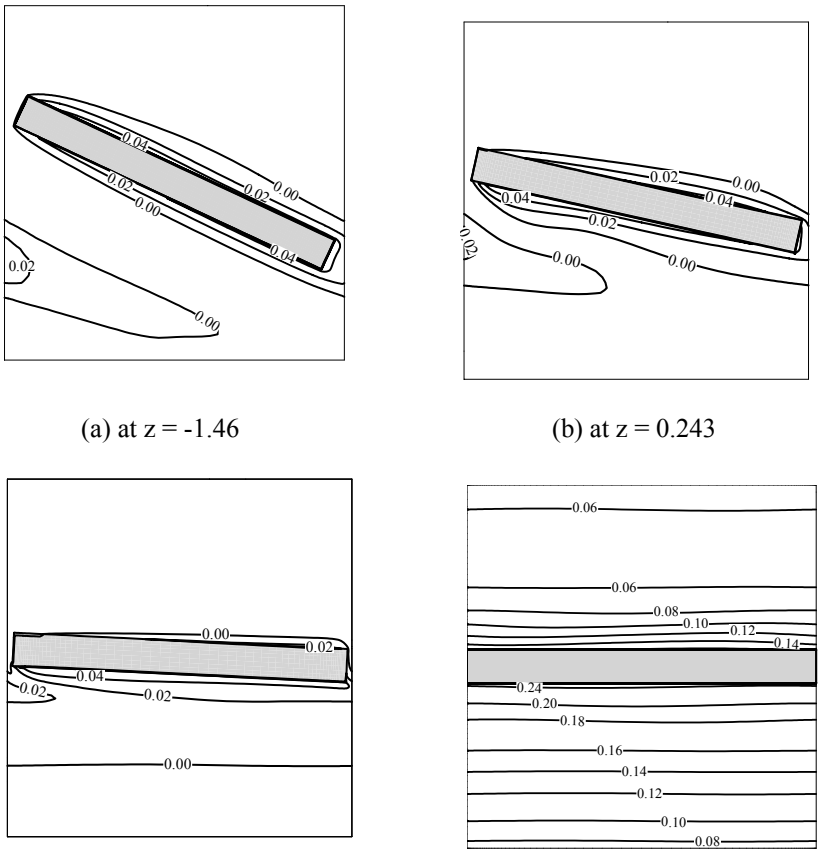

(a) at z = -1.46 (b) at z = 0.243

(c) at z = 0.424 (d) at z = 0.716

Figure 1.10. Mean thermal fields in four *z*- planes, (a) on the angled louver portion; (b) at the middle of the transition region; (c) near the flat landing; (d) on the flat landing.

Figure 1.11(a-b) plots the time mean thermal field on the top and bottom surface of the louver. A high surface temperature implies low heat transfer. On the top surface of the angled louver, the temperatures are lowest in the leading edge region, and increase as we travel downstream up to the mean reattachment line which occurs at about $x = 0$. Downstream of the mean reattachment line, the temperatures decrease due to the enhancement provided by spanwise vortices. On the lower surface, the temperatures are lowest in the vicinity of the leading edge and increase downstream. In the transition region, the mean temperatures follow the major unsteady flow features, outlined in the previous section. The high heat transfer region on the top surface near the flat landing is caused by the flow acceleration in the vicinity of the louver surface. On the other hand, a low heat transfer region is formed on the bottom surface due to the presence of the vortex jet. The low heat transfer region near the leading edge is a result

of a mean recirculation zone formed underneath the jet. On the flat landing, near the tube surface, the mean heat transfer is much higher on the top surface than the bottom surface.

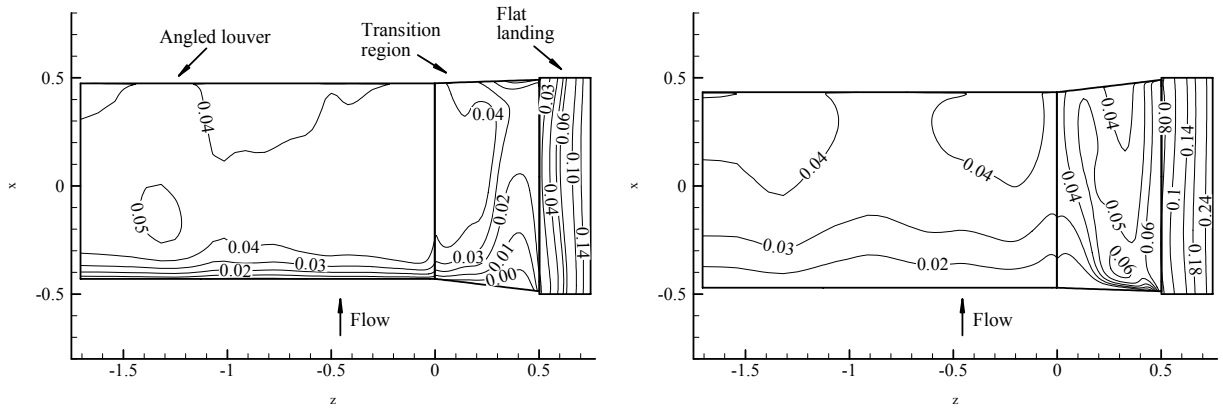

(a) Top louver surface

(b) Bottom louver surface

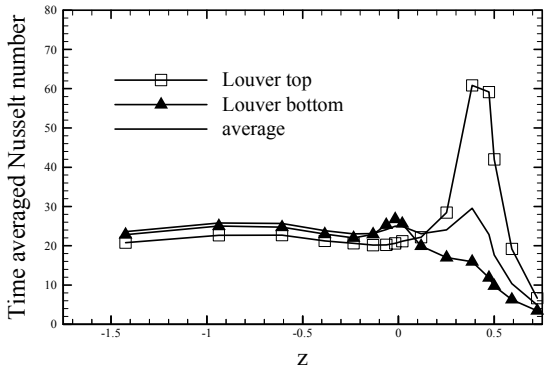

(c)

Figure 1.11. Mean thermal field distribution (a) on the top and (b) bottom surface of louver; (c) time averaged mean Nusselt number distribution along the fin height averaged over time 4.5-9.

Figure 1.11(c) plots the variation of local mean Nusselt number across the fin height. The results are averaged from $t = 4.5$ to 9. The Nusselt number is fairly constant on the angled louver up to the beginning of transition. As expected, in this region the Nusselt number is higher on the bottom surface, because of flow impingement and the absence of a mean recirculation region. In the transition region, the Nusselt number drops gradually on the lower surface but increases sharply on the top surface to more than twice its value. On the flat landing the Nusselt number drops to 4.1 and 7.3, respectively, on the bottom and top surface of the louver near the tube.

The mean Nusselt number integrated over the part of the louver simulated in the current study was found to be 22.7. On the tube surface the corresponding mean Nusselt number was calculated to be 7.2. Although, the transition region does provide some augmentation of heat transfer on the louver surface, its overall impact on louver heat transfer is limited because of its small spatial extent. However, the transition geometry does have a positive impact on tube heat transfer. In a separate calculation, which extended the angled louver to the tube surface, and

which excluded the transition and flat landing, found that the Nusselt number on the tube surface was lower by a factor of 1.5.

5. Conclusions

The flow and heat transfer in a three-dimensional geometry of a multilouvered fin is studied. The geometry includes the angled part of the louver and its transition to the flat landing along the fin height. Although the results shown here correspond to one Reynolds number for a given geometry, we believe that qualitatively the flow and heat transfer will show similar characteristics for other geometries as well.

The flow on the angled louver is characterized by spanwise vortex structures which are shed from the separated shear layers on the top and bottom surface of the louver. The flow is nominally two-dimensional with weak three-dimensionality. There is considerable interaction between vorticity shed from the leading edge of the louver and that formed in the wake of the louver. There is also strong evidence of interactions with vortices shed from upstream louvers. Vortices shed from the leading edge have a spatial life span between 3-4 louver lengths before they dissipate.

In the transition region, the flow is strongly three-dimensional and unsteady. It is characterized by strong streamwise flow velocities in the vicinity of the top louver surface near the junction with the flat landing and the formation of a vortex jet underneath the louver. There is evidence that the temporal evolution of the two are correlated. Both the high velocity region and the vortex jet oscillate on a short as well as a long time scale. However, the long time scale or low frequency oscillations are much stronger and persist for a longer time. It is suspected that both time scales are related to the formation and detachment of the vortex jet from the leading edge region. The flow characteristics isolated in the transition region will play a potentially important role in condensate carryover because of the high induced shear stresses.

In spite of the high heat transfer in this region, the overall effect on louver mean heat transfer is small because of the small spatial extent of the transition region. But, the strong acceleration near the junction with the flat landing does improve tube surface heat transfer by over 50 % when compared to a geometry in which the angled louver extends all the way to the tube surface.

6. References

[1] D.K. Tafti, L. Zhang, and G. Wang, Time-dependent calculation procedure for fully developed and developing flow and heat transfer in louvered fin geometries, *Numerical Heat Transfer*, *Part A*, 35, pp. 225-249, 1999.

[2] D.K. Tafti, X. Zhang, W. Huang, and G. Wang, Large-eddy simulations of flow and heat transfer in complex three-dimensional multilouvered fins, Invited paper, paper No. FEDSM2000-11325, CFD Applications in Automotive Flows, 2000 ASME Fluids Engineering Division Summer Meeting, June 11-15, Boston, Massachusetts, 2000.

[3] C.J. Davenport, Heat Transfer and Flow Friction Characteristics of Louvered Heat Exchanger surfaces, *Heat Exchangers: Theory and Practice*, Taborek, J., Hewitt, G. F. and Afgan, N. (eds.), pp. 397-412, Hemisphere, Washington, D. C., 1983.

[4] R.L. Webb, and P. Trauger, Flow structure in the louvered fin heat exchanger geometry, *Experimental Thermal and Fluid Science*, 4, pp. 205-217, 1991.

[5] X. Zhang, and D.K. Tafti, Classification and effects of thermal wakes on heat transfer in multilouvered fins, *Int. J. of Heat Mass Transfer*, 44, pp. 2461-2473, 2001.

[6] D.K. Tafti, and X. Zhang, Geometry effects on flow transition in multilouvered fins — onset, propagation, and characteristic frequencies, *Int. J. of Heat Mass Transfer* 44, pp. 4195-4210, 2001.

[7] D.K. Tafti, G. Wang, and W. Lin, Flow transition in a multilouvered fin array, *Int. J. of Heat Mass Transfer*, 43, pp. 901-919, 2000.

[8] L.W. Zhang, D.K. Tafti, F.M. Najjar, and S. Balachandar, Computations of flow and heat transfer in parallel-plate fin heat exchangers on the CM-5; effects of flow unsteadiness and three-dimensionality, *Int. J. of Heat Mass Transfer*, 40, pp. 1325-1341, 1997.

[9] L.W. Zhang, S. Balachandar, D.K. Tafti, and F.M. Najjar, Heat transfer enhancement mechanisms in inline and staggered parallel-plate fin heat exchangers, *Int. J. of Heat Mass Transfer*, 40, pp. 2307-2325, 1997.

[10] L.W. Zhang, S. Balachandar, and D.K. Tafti, Effect of intrinsic three dimensionality on heat transfer and friction loss in a periodic array of parallel plates, *Numerical Heat Transfer*, *Part A*, 31, pp. 327-353, 1997.

[11] D. Halt, personal communication, Visteon Automotive Systems, 1999.

[12] W.J. McLaughlin, and R.L. Webb, Condensate drainage and retention in louver fin automotive evaporators, SAE Technical Paper, 2000-01-0575, 2000.

[13] E.M. Sparrow, and A. Hajiloo, Measurements of heat transfer and pressure drop for an array of staggered plates aligned parallel to an air flow, *J. Heat Transfer*, 102, pp. 426-432, 1980.

[14] F.N. Beauvais, An aerodynamic look at automobile radiators, SAE Paper No. 65070, 1965.

[15] L.W. Zhang, personal communication, Modine Manufacturing Company, 2000.

[16] S.V. Patankar, C. H. Liu, and E. M. Sparrow, Fully developed flow and heat transfer in ducts having streamwise-periodic variations of cross-sectional area, *J. of Heat Transfer*, 99, pp. 180-186, 1977.

[17] J. Kim, and P. Moin, Application of a fractional step method to incompressible Navier-Stokes, *J. Comput. Phys.*, 59, pp. 308-323, 1985.

[18] Y.-J. Chang and C.-C. Wang, A generalized heat transfer correlation for louvered fin geometry, *Int. J. Heat Mass Transfer*, Vol. 40, No. 3, pp. 533-544, 1997.

[19] M.S. Chong, A.E. Perry, and B.J. Cantwell, A general classification of three-dimensional flow fields, *Physics of Fluids A* 2(5), pp. 765-777, 1990.

[20] F.M. Najjar, and S. Balachandar, Low-frequency unsteadiness in the wake of a normal flat plate, *J. Fluid Mech.*, 370, pp. 101-147, 1998.

[21] S. Mochizuki, and Y. Yagi, Characteristics of vortex shedding in plate arrays, in Flow Visualization II, ed. W. Merzkirch, Washington, D.C., Hemisphere, pp. 99-103.

Chapter 2. Fin-Tube Junction Effects on Flow and Heat Transfer Characteristics

Abstract

Three-dimensional simulations of four louver-tube junction geometries are performed to investigate the effect on louver and tube friction and heat transfer characteristics. Three Reynolds numbers, 300, 600 and 1100, based on bulk velocity and louver pitch are calculated. Strong three-dimensionality exists in the flow structure in the region where the angled louver transitions to a flat landing adjoining the tube surface, whereas the flow on the angled louver far from the tube surface is nominally two-dimensional. Due to the small spatial extent of the transition region, its overall impact on louver heat transfer is limited, but the strong unsteady flow acceleration on the top louver surface augments the heat transfer coefficient on the tube surface by over 100%. In spite of the augmentation, the presence of the tube lowers the overall Nusselt number of the heat exchanger between 25-30%. Comparisons with correlations derived from experiments on full heat exchanger cores show that computational modeling of a small subsystem can be used reliably to extract performance data for the full heat exchanger.

Nomenclature

D_H^*	Hydraulic diameter of equivalent duct
F_d^*	Flow depth
F_p	non-dimensional fin pitch (F_p^*/L_p^*)
L_p^*	dimensional louver pitch (characteristic length scale)
Nu	Nusselt number, $\dfrac{L_p^* q''^* / (T_s^* - T_{ref}^*)}{\kappa}$
Nu_{D_h}	Nusselt number, $\dfrac{D_h^* q''^* / (T_s^* - T_{ref}^*)}{\kappa}$
Pr	Prandtl number
q''^*	specified heat flux
Re	Reynolds number ($u_b^* L_p^*/\nu$)
Re_{L_p}	Reynolds number ($V_c^* L_p^* / \nu$)
Re_{D_h}	Reynolds number ($V_c^* D_H^* / \nu$)
T_s^*	louver or tube surface temperature
T_{ref}^*	reference temperature, domain integrated mixed mean
t	non-dimensional time
u_b^*	mean bulk velocity
V_c^*	maximum mean flow velocity
x	streamwise coordinate, along louver pitch
y	cross-stream coordinate, along fin pitch
z	lateral coordinate, along fin height

Greek symbols

γ	mean temperature gradient in the streamwise direction
κ	thermal conductivity
ν	kinematic viscosity
θ	non-dimensional modified temperature. Also louver angle

Superscripts

* dimensional quantities.

1. Introduction

Flat tube corrugated multilouvered fins are used in many compact heat exchanger applications to enhance the air-side heat transfer performance. Louvers reduce the average thermal boundary-layer thickness by interrupting its growth and by enhancing mixing through large-scale instabilities, hence increasing the average heat transfer coefficient. Previous experimental and numerical studies have established that the heat transfer in multilouvered fins is influenced by three factors: a) flow direction [1,2]; b) thermal wake interference [3]; c) flow instabilities and transport of coherent vorticity in the vicinity of the louver surface [4]. These three mechanisms have mostly been studied with a louver-centric view, i.e, heat transfer enhancement on a nominally two-dimensional louver, with the assumption that louvers contribute a significant portion to the overall heat transfer surface. For the most part this assumption is well justified. However, in exchangers with large fin pitches and small fin heights or tube pitch, the tube surface can contribute substantially to the total heat transfer. For example for a fin pitch of 1.5-2.0 times the louver pitch, and a tube pitch of 5 louver pitches, the tube surface area contributes between 20 to 30 percent of the total heat transfer area. This, coupled with the fact that the tube is the primary heat transfer surface with the largest potential for heat transfer, requires that attention be paid to the heat transfer from the tube surface.

Our specific geometry of interest is a flat tube multilouvered exchanger with corrugated rectangular channels. In order to gain some insight into what influences tube heat transfer, in this study we focus our attention on the region of the louver near the junction with the tube surface. In this region, along the height of the fin, the louver transitions from an angle θ to 0 degrees into a flat landing adjoining the tube surface as shown in Figure 2.1(d)[5]. Cui and Tafti [5] numerically investigated the geometry in Figure 2.1(d) at a Reynolds number of 1,100, based on louver pitch and bulk velocity. They found that although the flow on the angled portion of the louver was nominally two-dimensional with self-sustained flow oscillations characterized by spanwise vortices, the flow was strongly three-dimensional and unsteady in the transition region. An energetic unsteady vortex jet formed at the leading edge, which was drawn under the louver. The jet was complemented by a region of strong unsteady flow acceleration in the vicinity of the top louver surface. Evidence was presented that the temporal evolution of the two was correlated, which had a significant impact on local heat transfer coefficients. In spite of the high heat transfer in this region, the overall effect on mean louver heat transfer was found to be small because of the small spatial extent of the transition region. However, it was found that the strong acceleration near the junction with the flat landing had a significant effect on tube heat transfer.

[5] The corrugated fin curvature near the tube wall is neglected.

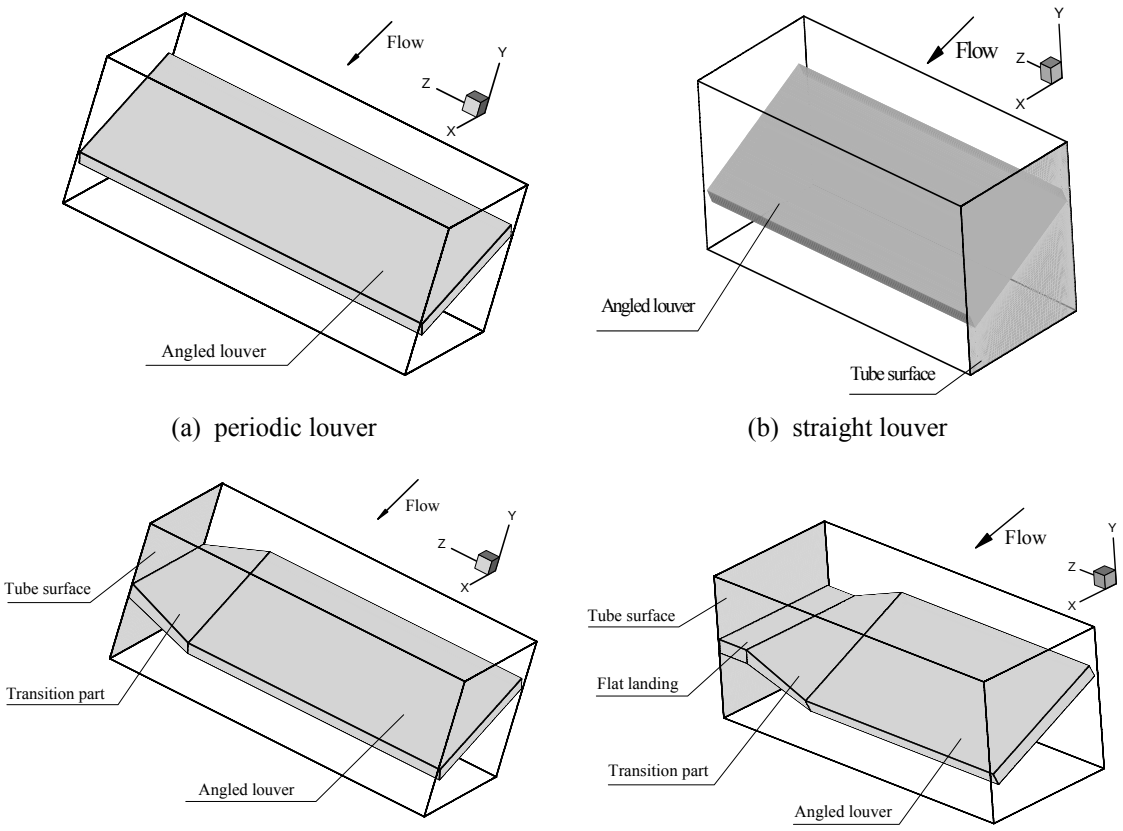

(a) periodic louver (b) straight louver

(c) transition without landing (d) transition with landing

Figure 2.1. Computational domain for four louver geometries: (a) periodic louver; (b) straight louver; (c) transition without landing; (d) transition with landing. Shaded areas are the louver and tube surface.

Our research objective is to study the three-dimensional flow and temperature fields generated in compact heat exchangers and to determine whether these largely unknown characteristics can be used to further augment heat transfer by slight modifications to the base geometries. The objective of this paper is to extend the previous three-dimensional unsteady simulations to study three Reynolds numbers, 1,100, 600 and 300. In addition to the Reynolds number effect, simulations are carried out on four variations of the transitional louver geometry to study the incremental effect of geometry at the junction with the tube. The heat transfer and friction results are presented separately for the louver and tube, and combined to estimate the overall effect. Comparisons are also made with existing louver-and-tube correlations in the literature to determine whether computational modeling of a subsystem can be used reliably to predict full heat exchanger core performance.

The paper is organized as follows: the numerical and computational method is presented briefly in the next section, followed by the description of the louver geometries. In the section on results, the general flow features, louver and tube friction and heat transfer characteristics are discussed. Finally comparisons are made with experimental correlations. This is followed by concluding remarks.

2. Numerical formulation

We solve the non-dimensional, time-dependent, incompressible Navier-Stokes and energy equations in conservative form in generalized curvilinear coordinates. The governing equations for momentum and energy are discretized with a conservative finite volume formulation using a second-order central difference scheme on a non-staggered mesh. The Cartesian velocities, pressure, and temperature are calculated and stored at the cell center, whereas contravariant fluxes are stored and calculated at the cell faces. A projection method [6] is used for the time integration of the discretized continuity and momentum equations.

The louvered fin geometry is approximated by an infinite array of louvers in both streamwise and cross-stream directions, which results in a simpler system with periodic repetition of the basic unit. Periodic boundary conditions for velocity, modified pressure and temperature are applied in the streamwise and cross-stream directions since the flow is assumed to be both hydrodynamically and thermally fully developed without any entrance or exit effects. No-slip, no-penetration boundary conditions for velocity and constant heat flux conditions are enforced on the louver and tube surface.

More details of the numerical algorithm, treatment of the boundary conditions, verification and validation of the computer program and strategies for parallel computing can be found in Tafti et al. [7,8,9] and Cui and Tafti [5].

3. Description of four louver geometries

Four louver geometries are considered in this paper (see Figure 2.1): (1) periodic louver; the louver is assumed periodic in the spanwise direction with no tube. This simulation isolates any intrinsic three-dimensional effects brought about by secondary three-dimensional instabilities [10]; (2) straight louver; the angled louver extends all the way to the tube; this serves as a baseline case to study the effect of louver geometry transition; (3) louver with transition without landing; the angled louver directly transitions to the tube surface; (4) louver with transition and flat landing, which has been studied in detail by Cui and Tafti [5] at Re=1100. Comparison of (3) and (4), highlights the role of the flat landing.

For all four geometries, the unit computational domain has a dimension of 1 (normalized by louver pitch L_p^*) in streamwise (x) direction, fin pitch 1 (in this particular case, fin pitch F_p^* is same as L_p^*) in cross-stream (y) direction, and 2.5 in spanwise (z) direction along the fin height. Along the spanwise direction in geometry 4 (hereafter referred as *transition with landing*), the louver can be divided into three parts: angled louver (length, 1.75), transition part (length, 0.5), and flat landing (length, 0.25). A linear transition profile is prescribed between the angled louver and the flat landing with a small radii of curvature at the junction with the louver [11]. For geometry 3 (hereafter referred to as *transition without landing*), the angled louver part is extended to a length of 2.0, and the transition part is unchanged, but the flat landing between the transition and the tube surface is removed. Geometry 2, referred to as a *straight louver*, has a spanwise extent of 2.5. Finally, geometry 1 is referred to as a *periodic louver* and has a spanwise extent of 2.5.

In all cases, the thickness of the angled louver is 0.1 times the louver pitch with 25° louver angle. For the last three geometries, symmetry boundary conditions are imposed at a distance of 2.5 from the tube surface along the fin height, assuming that the flow is sufficiently removed from the extrinsic three-dimensional effects of the tube wall region and is nominally two-dimensional. This also assumes implicitly that the fin height is 5.0 louver pitches.

For the periodic louver, periodic boundary conditions are implemented in the spanwise direction since the flow is homogeneous along this direction.

The computational domain surrounding each louver is resolved by 98x98x128 computational cells in the *x*-, *y*- and *z*- directions, respectively for the transitioning geometries. For the periodic and straight louver, 96 computational cells are used in the *z*- direction along the fin height. A very fine, nearly orthogonal mesh, is used in the vicinity of the louver and tube surface, and in the transition region [5]. *A-posteriori* extraction of the mean wall shear stress for Re=1100 shows that the first grid point near the louver surface falls between 0.1 and 0.3 in local wall units based on the local shear stress. In the region with the largest shear stress (in the transition region), there are five grid points within 10 wall units normal to the surface, with the first at 0.3. Along the streamwise direction, the grid is nearly uniform with spacing of 5-7 wall units. Along the fin height or spanwise direction, the mesh is coarsest in the two-dimensional region of the geometry with the maximum spacing of 60 wall units and finest at the beginning and end of transition, and near the tube wall with spacing around 3 wall units. Spectral analyses show that the spatial and temporal resolution is fine enough to capture all the relevant scales in these calculations [5].

4. Results

In each of the calculations, a mean non-dimensional pressure gradient of unity is imposed in the streamwise direction to drive the flow. As the calculation proceeds, the flow rate, in response to the frictional and pressure drag losses in the calculation domain, adjusts to the mean pressure gradient and reaches a stationary (or steady state, in the case of low Reynolds number steady flow). Time signals of flow variables are recorded and a stationary flow is assumed when a near constant mean value or a quasi-periodic fluctuation in time is observed. Figure 2.2 shows the temporal evolution of the spatially averaged Nusselt number for four louver geometries at a nominal Reynolds number of 1,100. It is clear that all flows have adjusted to the mean pressure gradient and reached a statistically stationary state. Similar plots at nominal bulk Reynolds number of 600 and 300 also show that the flow has reached a stationary or steady state.

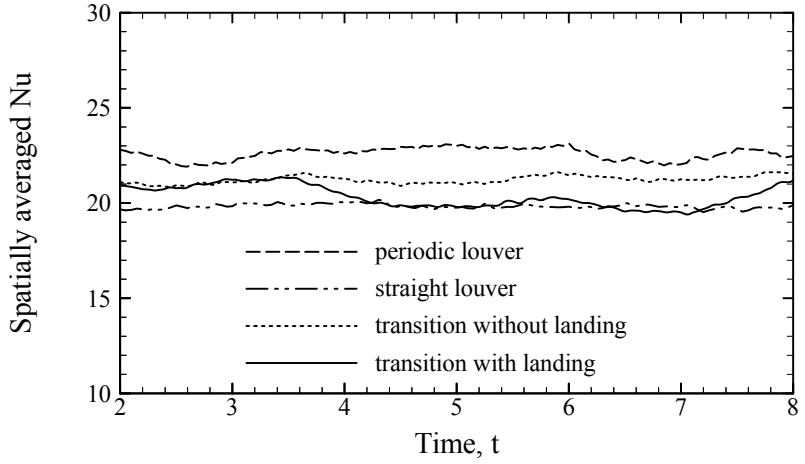

Figure 2.2. Temporal evolution of the spatially averaged Nusselt number for four louver geometries at Reynolds number of 1,100. All flows have adjusted to the mean pressure gradient and reached a statistically stationary state. Similar plots at Reynolds number of 600 and 300 also show that the flow has reached a stationary state.

To characterize the heat transfer, we define a local instantaneous Nusselt number over the louver/tube surface based on the louver pitch as

$$Nu = \frac{L_p^* q''^* / (T_s^* - T_{ref}^*)}{\kappa}$$

In terms of non-dimensional quantities the above can be re-written as

$$Nu = \frac{1}{\theta_s - \theta_{ref}}$$

where θ_s [6] is the modified non-dimensional surface temperature and θ_{ref} is the reference modified non-dimensional bulk temperature, which is defined as :

$$\theta_{ref} = \frac{\iint |u| \theta dA_x}{\iint |u| dA_x}$$

The surface-averaged Nusselt number is obtained by integration over the louver or tube surface as:

$$Nu = \frac{\iint_{\Omega} d\Omega}{\iint_{\Omega} (\theta_s - \theta_{ref}) d\Omega}$$

where Ω denotes the louver or tube surface. The Colburn j factor as a measure of heat transfer is calculated as:

$$j = \frac{Nu}{\mathrm{Re}\,\mathrm{Pr}^{0.4}}$$

The Fanning friction coefficient is calculated as:

$$f = \frac{\Delta p^*}{\frac{1}{2}\rho V_c^{*2}} \frac{D_h^*}{4F_d^*} = \frac{D_h}{2} \frac{1}{V_c^2}$$

where D_h^* is the hydraulic diameter, $\Delta p^* / F_d^*$ is the prescribed pressure gradient across the calculation domain (unity non-dimensional value in present calculations), and V_c^* is the calculated maximum mean velocity.

4.1 General Flow Features

In the study of the louver with transition and flat landing [5], it is shown that flow on the angled louver portion is characterized by periodic spanwise vortex shedding at the Reynolds number of 1,100. The spanwise vortices are nominally two-dimensional in nature with weak three-dimensionality across the fin height. The time signal at a location above the top louver surface exhibits a nearly periodic pattern, and the frequency spectrum shows a clear peak at 1.8 (non-dimensionalized by bulk velocity and louver pitch), which corresponds to the frequency of the spanwise vortex shedding. At this Reynolds number of 1,100, all four louver geometries exhibit the same vortex shedding characteristic frequency. Although there is considerable geometry variation near the tube surface, its effects on the flow field on the louver away from the tube is minimal. Because of these similarities at the

[6] $T(x,y,z,t) = T_{in} + \gamma x + \theta(x,y,z,t)$, where γ is the mean temperature gradient.

angled louver part, nearly identical flow and heat transfer behavior is expected for the four louver geometries. Any observable differences would come from the area near the tube surface.

At Reynolds number of 600, the flow unsteadiness becomes much weaker at the angled louver part. The time signals do not show a periodic pattern, and vortex shedding only occurs in an occasional manner, and there is no clear characteristic frequency. At Reynolds number of 300, the flow is completely steady and remains attached on the louver surface and there is no evidence of vortex shedding for all louver geometries. These results are in agreement with a previous two-dimensional investigation on the onset of instabilities for developing flow in a louver bank [4].

To facilitate our understanding of the unsteady nature of the flow and the associated vorticity dynamics, the $\nabla \boldsymbol{u}$ [12] vortex identification technique is used. This frame-invariant method identifies vortical structures as regions of large vorticity, where rotation dominates over strain to cause the rate-of-deformation tensor $\nabla \boldsymbol{u}$ (velocity gradient tensor) to have complex eigenvalues (one real and two conjugate complex eigenvalues). The complex eigenvalues imply that the local streamline pattern is closed or spiral, thus correctly eliminating near-wall shear layers. This methodology can also be separately applied in the *x*-, *y*-, or *z*- planes in order to identify streamwise, cross-flow, and spanwise vortices [10], respectively. The strength of the vortex is measured in terms of the imaginary part of the eigenvalue of the velocity gradient tensor and is denoted by λ_i. The strength of its three subsets, streamwise, cross-flow, and spanwise vortices is measured in terms of the imaginary part of the eigenvalue of the velocity gradient on the *x*-, *y*-, and *z*- planes, respectively, and is denoted by $\lambda_{i,x}$, $\lambda_{i,y}$, and $\lambda_{i,z}$, respectively.

Figure 2.3(a-d) shows the volume-averaged vortical strength $\lambda_{i,x,y,z}$ distribution along the fin height at an arbitrary instant at Reynolds number of 1,100[7]. Only the volumes with non-zero eigenvalues are included in the volume averaging. For the periodic case (Figure 2.3-a), the lines for streamwise ($\lambda_{i,x}$) and cross-flow ($\lambda_{i,y}$) vorticity are identically zero throughout the louver height. The only contribution to the total vorticity is from the spanwise vorticity ($\lambda_{i,z}$). Hence at Re=1,100, for the given louver geometry, the flow is strictly two-dimensional and intrinsic three-dimensional secondary instabilities have not developed[8]. For the straight louver, (Figure 2.3-b), the spanwise vorticity dominates. However, there are small components of both streamwise ($\lambda_{i,x}$) and cross-stream ($\lambda_{i,y}$) vorticity present along the louver height. This implies that the three-dimensionality introduced by the presence of the tube wall permeates into the flow away from the wall and introduces weak three-dimensionality in a nominally two-dimensional flow. The spanwise vorticity ($\lambda_{i,z}$) is damped considerably by the viscous presence of the wall which is felt up to one louver pitch away from it, implying very thick boundary layers on the tube wall. Approaching the tube surface, there is a noticeable but slight increase for both streamwise ($\lambda_{i,x}$) and cross-flow ($\lambda_{i,y}$) vorticity as the spanwise and total vorticity decrease.

[7] To obtain the distribution, the volume averaging is performed in domains defined by decompositions used for parallel computation along the fin height.
[8] The nominally 2-D flow was perturbed by 3-D disturbances to seed any intrinsic three-dimensional secondary instabilities, but the perturbations were not self-sustaining.

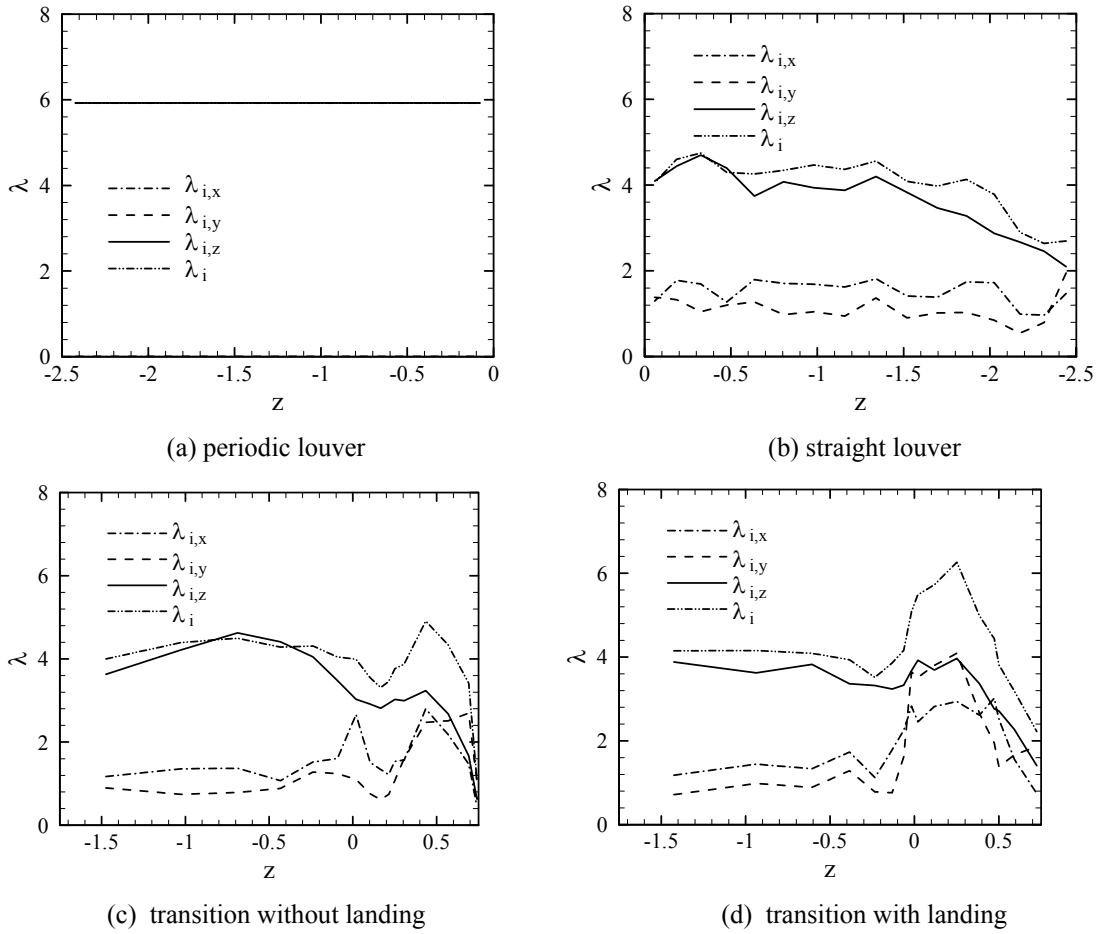

Figure 2.3. Instantaneous volume-averaged vortical strength distribution along the fin height at Reynolds number of 1,100 at an arbitrary instant for (a) periodic louver; (b) straight louver; (c) transition without landing; (d) transition with landing.

For the louver with transition and flat landing (Figure 2.3-d), on the angled louver, λ_i essentially maintains a constant value, with a dominant contribution from spanwise vorticity. However, in the transition region the flow is strongly three-dimensional. λ_i increases, with increasing contributions from streamwise and cross-stream vorticity, with a drop in contributions from spanwise vorticity. λ_i reaches a maximum in the center of the transition region and then decreases as the louver approaches the flat landing and the tube surface. The increase in the streamwise and cross-stream components of vorticity is related to the formation of an unsteady vortex jet under the bottom louver surface, which is described in detail in Cui and Tafti [5]. Not reflected in these plots, but related to the vortex jet, is the formation of a highly unsteady region of accelerated flow velocities on the top surface of the louver. For transition without landing (Figure 2.3-c), it is seen that the magnitude of coherent vorticity in the transition region is reduced. This is because, in the presence of the flat landing the fluid acceleration on the top surface and the vortex jet feed off the streamwise flow along the flat landing. In the absence of the flat landing, when the louver transitions directly to the tube surface, there is reduced access to fluid mass, which results in the weakening of these flow structures.

4.2 Pressure and Friction Drag on Louver and Tube

Figure 2.4(a-d) plots the *fractional* variation of mean form and friction drag per unit length along the fin height or spanwise direction at a nominal Re = 1,100[9]. For all four geometries, at the angled louver portion, the form drag dominates the friction drag and is almost unchanged throughout the angled louver. This is best exemplified by the two-dimensional flow over the periodic louver in Figure 2.4(a), in which the form drag contributes 80 % to the overall pressure loss. For transition with landing (Figure 2.4-d), and transition without landing (Figure 2.4-c), the magnitude of pressure and friction drag is similar at the angled louver part. For the straight louver, although the form drag loss is four times the friction losses away from the tube surface, which is similar to other geometries, the contribution to total losses is dominated by the presence of the tube. Both frictional and form losses increase substantially in the vicinity of the tube surface because of viscous effects. As the flow approaches the tube, it slows down, and the flow angle reduces substantially, which leads to the increased contribution to form drag. For the transitioning geometries in Figure 2.4(c) and (d), the trends are completely different. In the transition region, the form drag increases slightly and eventually vanishes at the flat landing. On the other hand, friction drag increases sharply in the transition region and reaches its largest value near the flat landing due to the accelerated high velocity boundary layer in that region before decreasing again on the flat landing. Similar, albeit weaker, distributions at the transition region are found for the transitioning geometry without the landing (Figure 2.4-c).

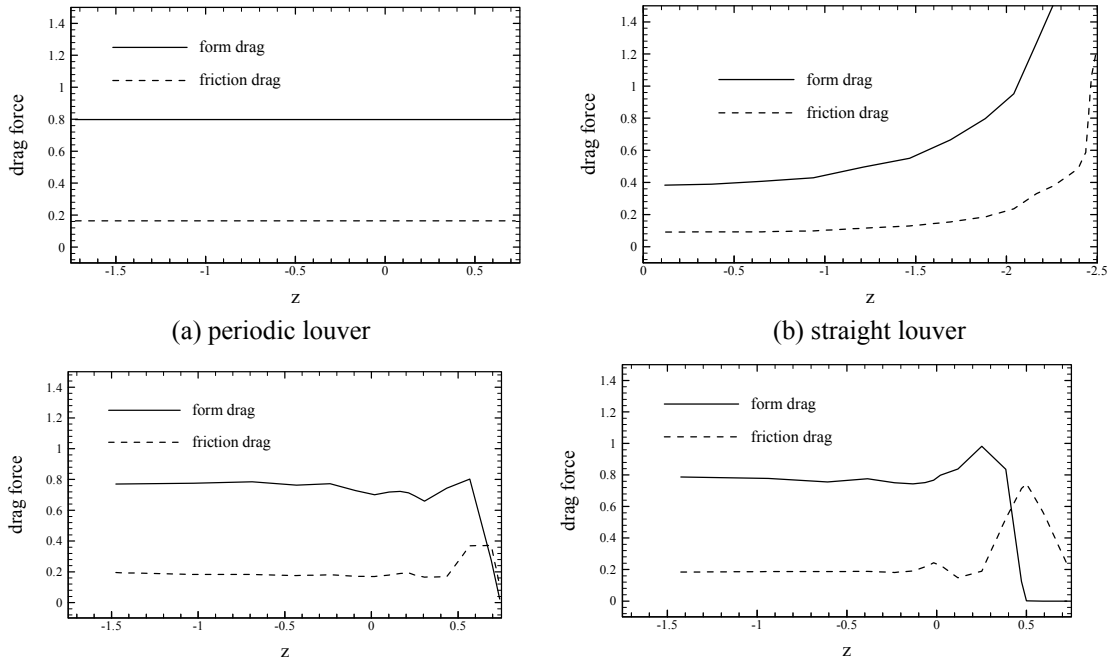

Figure 2.4. Mean drag force distribution along the fin height as a fraction of the total losses: (a) periodic louver; (b) straight louver; (c) transition without landing; (d) transition with landing at Reynolds number of 1,100.

[9] The form and friction drag are plotted as a fraction of the total losses. Since the mean pressure gradient is fixed at unity, the integrated area under the curves should add up to approximately (barring tube frictional losses) 2.5, the pressure loss expressed as a force on the computational domain.

Figure 2.5(a-c) plots the mean drag force distribution as a function of the fin height for the transition with landing geometry at three Reynolds numbers: 1,100, 600, and 300. As the Reynolds number decreases, the contribution of pressure drag decreases while that of friction drag increases at the angled louver part. At a nominal Reynolds number of 300, the two drag forces are nearly equal. The distribution at the transition region and flat landing follow the same trend as the Reynolds number decreases. Overall the changes in Reynolds number do not change the salient features of the drag distribution throughout the louver. This is also true for the other three louver geometries.

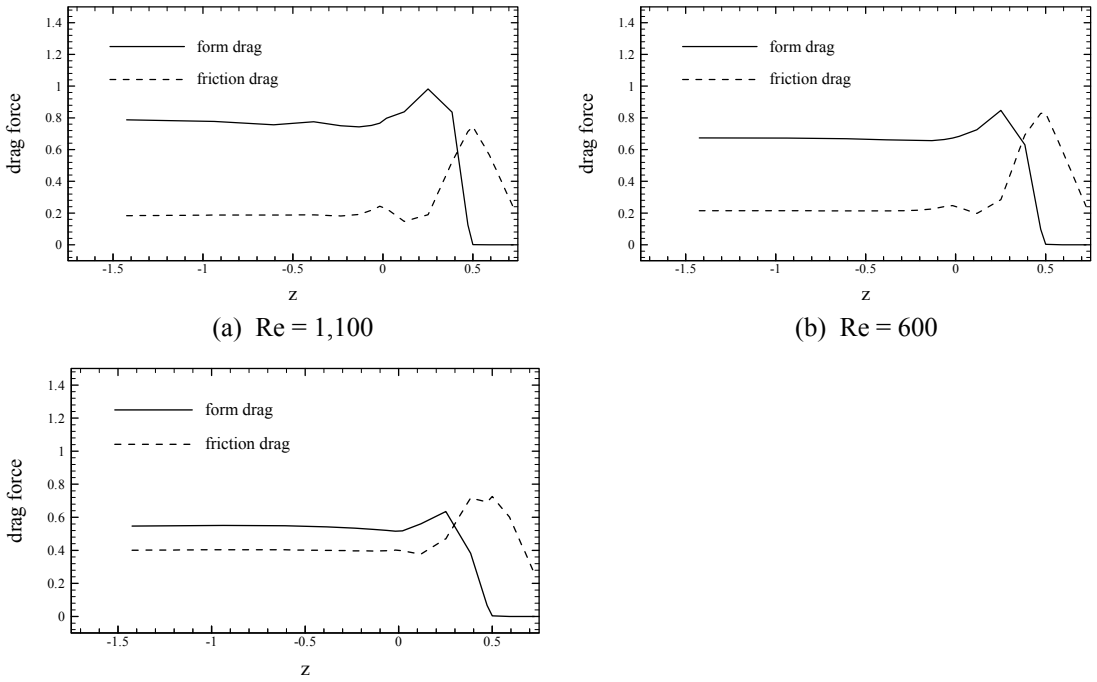

(a) Re = 1,100

(b) Re = 600

(c) Re = 300

Figure 2.5. Mean drag force distribution along the fin height as a fraction of the total losses for transition with landing at Reynolds number of (a) 1,100; (b) 600; (c) 300.

Figure 2.6 plots the fractional contribution of friction losses on the tube surface to the total losses. For all three geometries, the contribution of the tube to overall losses is less than 8 percent of the total. The louvers with transition exhibit a higher contribution because of the increased shear stress on the tube surface as a result of the unsteady accelerating boundary layer in the vicinity.

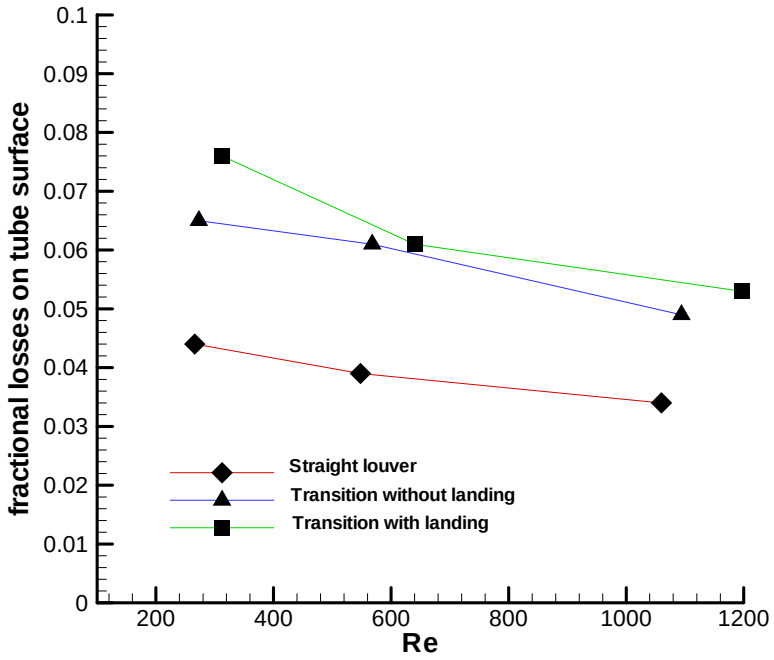

Figure 2.6. Fractional contribution of friction on tube surface to overall pressure loss.

4.3 Time-averaged Heat Transfer Coefficient

Figure 2.7(a-d) plots the time mean thermal field (modified temperature, θ) on the top surface of the louver. Because the heat flux is fixed on the louver and tube surface, a high surface temperature implies low heat transfer. In all cases, at a nominal Re =1100, the shear layer at the leading edge of the louver separates and sheds vortices. Very near the leading edge, the heat transfer coefficients are high, but decrease in the recirculation zone which forms downstream of the leading edge. In the reattachment region, at half the louver length, the vorticity generated by the separated shear layer increases the heat transfer coefficient by increasing mixing. For the periodic geometry, in the absence of any extrinsic three-dimensionality, the surface temperature does not show any variations in the z-direction. For the straight louver, the thick thermal boundary layer on the tube surface dominates the temperature distribution on the top surface. For transition with landing, in the transition region, the low temperature/high heat transfer region on the top surface near the flat landing is a result of the unsteady accelerating boundary layer on the louver surface. Similar trends are observed for the transitioning louver with no landing.

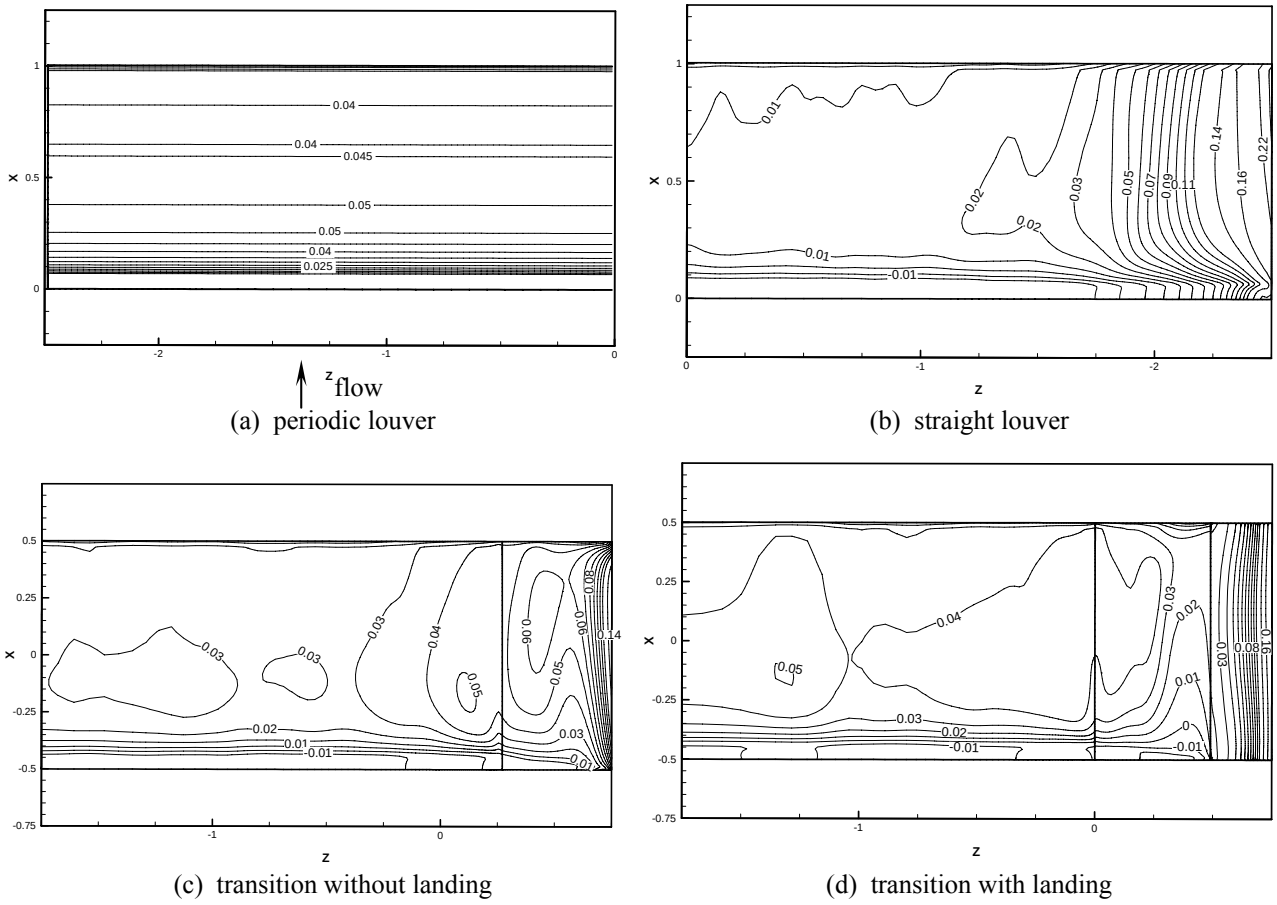

Figure 2.7. Mean thermal field distribution on the louver top surface at Reynolds number of 1,100 for (a) periodic; (b) straight louver; (c) transition without landing; (d) transition with landing.

Temperature contours on the lower surface are shown in Figure 2.8(a-d). For the periodic louver the heat transfer coefficient is a maximum at the leading edge and decreases thereafter till near the trailing edge where it increases again. A high temperature/low heat transfer region formed in the transition region in Figure 2.8(c-d) results from the presence of the vortex jet. The jet is detached from the louver surface and a stagnant recirculating region is formed underneath the jet. Similar to the top surface, a thick boundary layer near the tube surface exists for the straight louver on the bottom surface. Comparing temperature contours on the top and bottom louver surfaces for both the transitional geometries in the vicinity of the tube clearly shows the positive effect of the accelerating boundary layer on the top surface. Temperature contours have lower values in the immediate vicinity of the tube on the top louver surface than on the bottom surface.

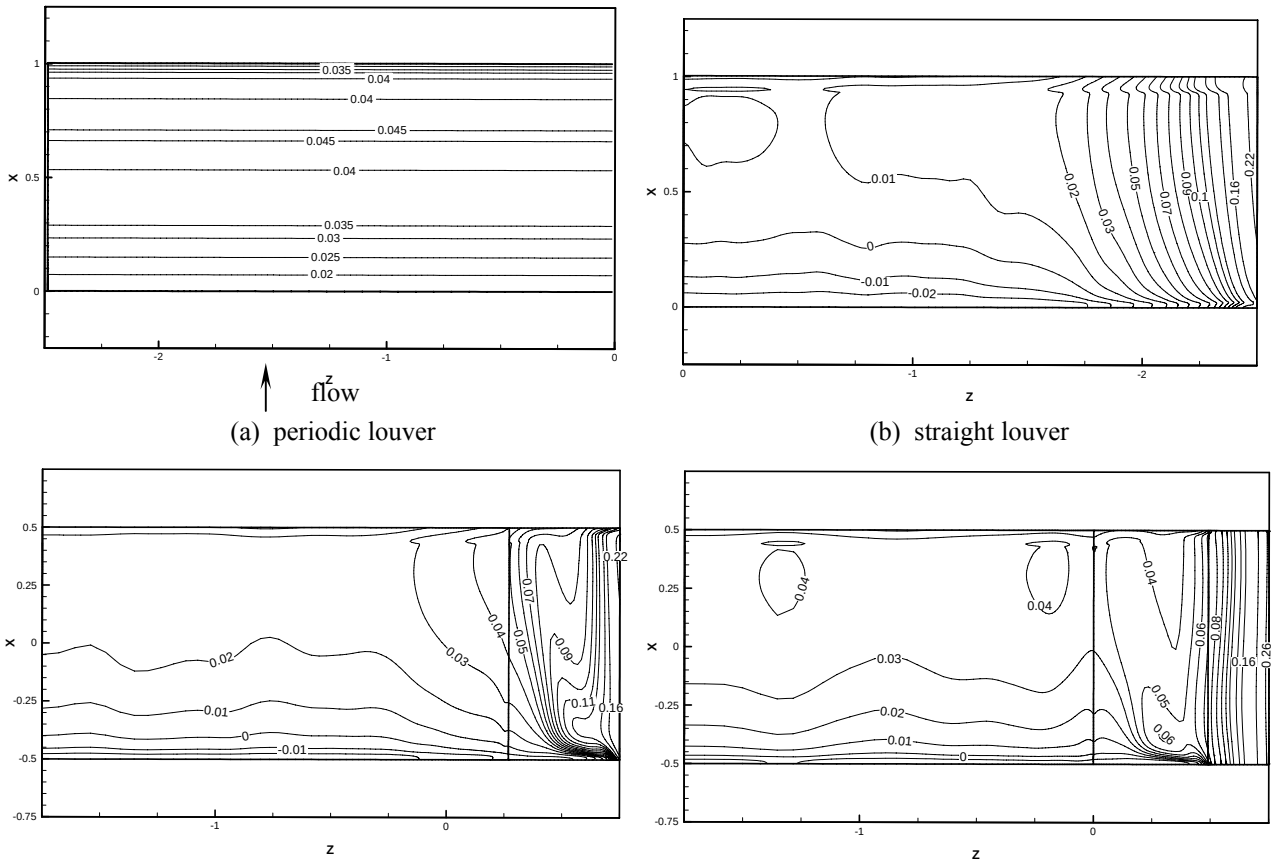

Figure 2.8. Mean thermal field distribution on the louver bottom surface at Reynolds number of 1,100 for (a) periodic; (b) straight louver; (c) transition without landing; (d) transition with landing.

In Figure 2.9(a-b), the average (time and spatial) Nusselt number on the louver, and tube surface is plotted separately. In general, the first order effect of the angled louver transitioning to zero degrees and a flat landing is to reduce the heat transfer coefficient. Also, the presence of the tube surface further reduces the heat transfer coefficient on the louver surface because of the presence of thick thermal boundary layers at the junction between fin and tube. These effects can either be countered or reinforced further by other non-linear effects as observed (unsteady boundary layer acceleration on louver top surface and vortex jet on bottom surface, separation) in the current study. The unsteady boundary layer acceleration on the top surface has a positive impact on louver heat transfer, whereas the formation of the vortex jet at the bottom has a neutral to negative impact. The results in Figure 2.9(a) are consistent with these observations. The periodic louver exhibits the highest heat transfer coefficient, whereas the straight louver and the transitioning louver with a flat landing exhibit heat transfer coefficients which are between 15-25% lower. The transitioning louver without a landing lies between the two extremes and is between 6-15% lower. These results indicate that to maintain a high heat transfer coefficient on a transitioning louver, the flat landing should be as small as physically possible.

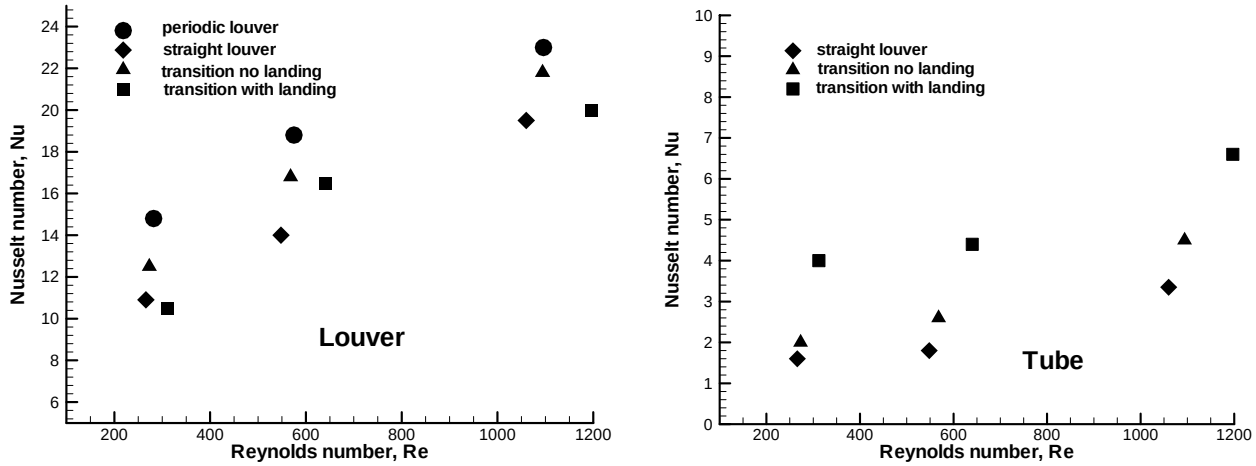

(a) (b)

Figure 2.9. Average Nusselt number versus the Reynolds number. (a) On the louver surface; (b) On the tube surface.

On the other hand, the enhancement provided by the transitioning louver with a flat landing on the tube surface is quite strong. The tube Nusselt number is lowest for the straight louver because there is nothing that can break the thick thermal boundary layer that forms at the fin-tube junction. With the transitional louver, the unsteady boundary layer acceleration on the top surface and to some extent the vortex jet under the louver, help to perturb and thin the thermal boundary layer on the tube and increase the heat transfer coefficient. Without the flat landing, the unsteady nature of the flow is considerably weakened as noted in Figure 2.3, and the augmentation on the tube surface is not as high. Transition with flat landing provides an augmentation of over a 100% over a straight louver, whereas with no landing, the augmentation is reduced to between 30-40%.

4.4 Overall Friction and Heat Transfer Coefficient for Flat Tube Louvered Heat Exchanger

In this section, the overall heat transfer and friction factors for an equivalent duct of aspect ratio 5, bounded by louvered fins and the tube surface are presented. These are compared to theoretical flow results for fully developed laminar flow in ducts. Figure 2.10-a compares the calculated friction coefficient (*f*), and Figure 2.10-b plots the equivalent Nusselt number (Nu_{D_h}) versus Re_{D_h} .

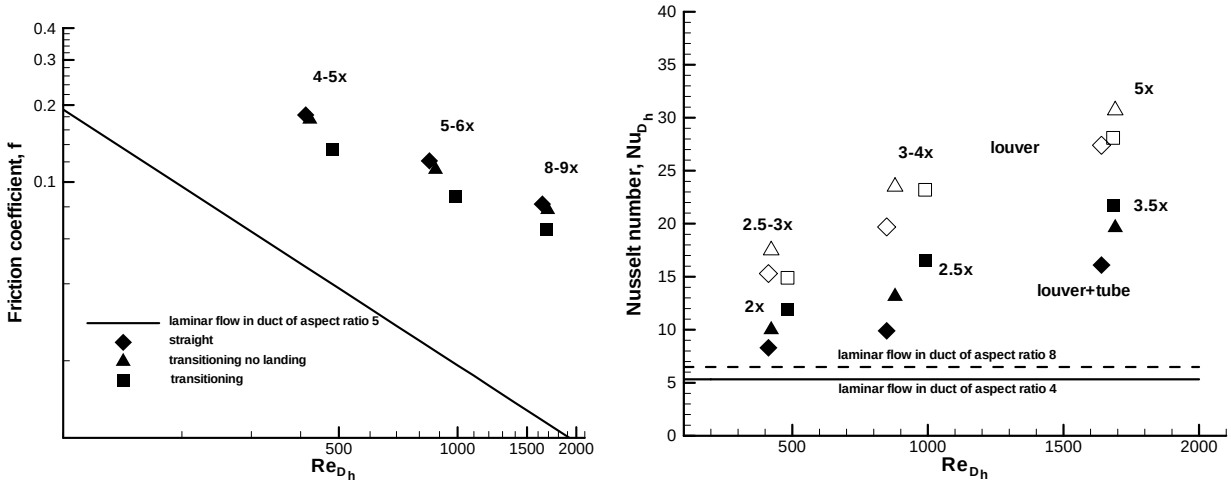

Figure 2.10. (a) Friction coefficient, *f* for equivalent louvered duct; (b) Nusselt number for equivalent louvered duct. *Diamond*: straight louver; *delta*: transition no landing; *square*, transition with landing. *Empty symbols*: Nusselt number based on louver surface; *filled symbols*: Nusselt number based on louver and tube surface.

The friction coefficient increases by a factor between 4 and 9 when compared to a fully-developed laminar flow in a duct of aspect ratio 5. On the other hand the Nusselt number is augmented by factors varying from 2 to 3.5. The tube surface results in approximately a 25-30% reduction in the overall Nusselt number. Hence, for small tube pitches and large fin pitches, tube surface heat transfer becomes critical to the performance of the heat exchanger. In fact, in spite of the louver heat transfer being highest for the geometry without a landing, the overall Nusselt number is highest for the geometry with a flat landing because of a larger heat transfer coefficient on the tube surface. Between the three geometries, the louver with transition and flat landing exhibits the lowest friction coefficient, whereas the friction coefficient is highest for the straight louver. The result goes against Reynold's analogy, but is consistent with the fact that losses are dominated by louver form drag, which is reduced substantially in the transition region and vanishes at the flat landing. This, together with the heat transfer augmentation provided on the tube surface with a minor increase in skin friction, is responsible for the above result.

Finally we provide a comparison between the calculated results and previous experimental work. Both the calculated friction coefficient and Colburn *j*-factor are compared to relevant correlations available in the literature. This is provided to validate that in spite of the simplifying assumptions inherent in computer models, and the geometrical imperfections in real exchanger cores on which experiments are performed, physically consistent models of a subsystem of the full heat-exchanger are capable of providing realistic performance measures of the full system. The friction coefficient is compared to the correlation of Chang et al. [13], (referred to as CHLW) and the *j*-factor to the correlation by Chang and Wang [14] (referred to as CH), and also to that of Sunden and Svantesson [15] (referred to as SS). The SS correlation is specific to flat tube arrangements with corrugated louvers in rectangular channels, whereas both the *f*- and *j*- correlations are more general in nature and include a wide range of multilouvered geometries [13]. The following geometrical values are used in the correlations: fin pitch = 1(all

lengths normalized by louver pitch), $\theta = 25$ degrees, fin thickness = 0.1, fin height = tube pitch = 5, tube depth = 15, louver length = 4.5, major tube diameter = 1[10], and louver height as $0.5\sin\theta$.

Figure 2.11(a-b) plot the *f*- and *j*- factor. Also plotted are upper and lower bounds of the experimental data from which the CHLW and CW correlations are derived. The calculated *f*- factor for all three cases falls within the upper bounds of the experimental data. We also note that the current calculations are relevant to the type C geometry in Chang and Wang [14], which generally exhibits a higher friction coefficient than the other types of multilouvered geometries. Similarly, the calculated *j*-factors for the transitioning louvers fall well within the experimental bounds of the CW correlation but are lower than the SS correlation. In both comparisons we find that the more realistic louver with a flat landing agrees best with the correlations.

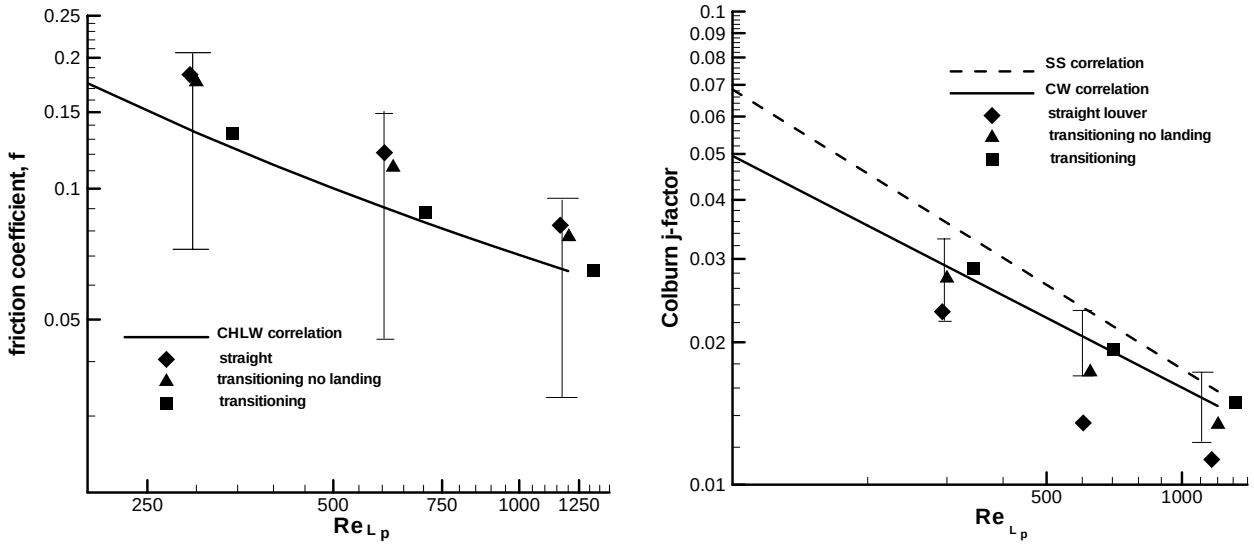

Figure 2.11. Comparison of calculated *f*- and *j*- factors with available correlations. Vertical lines establish limits of experimental data from which the CHLW and CH correlations were constructed.

5. Conclusions

In this paper, we study the flow and heat transfer in four three-dimensional geometries (Figure 2.1) of a flat tube corrugated multilouvered fins at three nominal Reynolds numbers: 1,100, 600, and 300. The four geometries vary in the configuration of the fin at the junction with the tube face. They range from completely neglecting the effect of the tube surface to including the realistic transition of the angled louver into a flat landing adjoining the tube face. The objective is to study the impact of this region on louver as well as tube heat transfer coefficients and to determine whether modeling a small subsystem (a single louver) is representative of the performance of the full heat exchanger core.

The results show that away from the tube surface, the flow is nominally two-dimensional with weak three-dimensionality. For louvers that flatten out into a flat landing, conditions are created for highly three-dimensional

[10] Tube depth is used in the same context as flow depth. In our calculations, the flow depth is infinity. So a typical value of 15 is used. Similarly, the calculations do not simulate flow around the tube, so a value of 1.0 is assumed as the major tube diameter. In any case, for flat tubes, the contribution to pressure loss from the frontal area of the tube is negligible.

and unsteady flow phenomena. Flow in the transition region is characterized by unsteady boundary layer acceleration on the louver top surface and a vortex jet under the louver bottom surface. The flow acceleration has a large impact on louver heat transfer locally. However, its impact is minimal on the averaged heat transfer coefficient over the whole louver. It is concluded that for best louver heat transfer performance, the transition and flat landing should be kept as small as possible. On the other hand, the boundary layer acceleration generated by the transitioning louver with a flat landing has a large impact on tube heat transfer and increases it by over 100% over a straight louver which does not transition to the tube surface.

It is found that the low heat transfer on the tube surface decreases the overall heat transfer capacity of the heat exchanger between 25-30%. Hence, augmenting heat transfer on the tube surface would have large payoffs in small tube pitch, large fin pitch, multilouvered geometries. On the other hand, there is a minimal contribution (<8%) of tube frictional losses to total losses.

The agreement of calculated results with correlations derived from full core experiments validates that realistic three-dimensional computational modeling of a small subsystem is a viable and effective tool in generating performance data for heat exchangers.

6. References

[1] C.J. Davenport, Heat Transfer and Flow Friction Characteristics of Louvered Heat Exchanger surfaces, *Heat Exchangers: Theory and Practice*, Taborek, J., Hewitt, G. F. and Afgan, N. (eds.), pp. 397-412, Hemisphere, Washington, D. C., 1983.

[2] R.L. Webb, and P. Trauger, Flow structure in the louvered fin heat exchanger geometry, *Experimental Thermal and Fluid Science*, 4, pp. 205-217, 1991.

[3] X. Zhang, and D.K. Tafti, Classification and effects of thermal wakes on heat transfer in multilouvered fins, *Int. J. of Heat Mass Transfer*, 44, pp. 2461-2473, 2001.

[4] D.K. Tafti, and X. Zhang, Geometry effects on flow transition in multilouvered fins — onset, propagation, and characteristic frequencies, *Int. J. of Heat Mass Transfer*, 44, pp. 4195-4210, 2001.

[5] J. Cui, and D.K. Tafti, Computations of flow and heat transfer in a three-dimensional multilouver fin geometry, *Int. J. Heat Mass Transfer*, to appear, 2002.

[6] J. Kim, and P. Moin, Application of a fractional step method to incompressible Navier-Stokes, *J. Comput. Phys.*, 59, pp. 308-323, 1985.

[7] D.K. Tafti, L. Zhang, and G. Wang, Time-dependent calculation procedure for fully developed and developing flow and heat transfer in louvered fin geometries, *Numerical Heat Transfer*, *Part A*, 35, pp. 225-249, 1999.

[8] D.K. Tafti, X. Zhang, W. Huang, and G. Wang, Large-eddy simulations of flow and heat transfer in complex three-dimensional multilouvered fins, 2000 ASME Fluids Engineering Division Summer Meeting, FEDSM2000-11325, FED Vol. 251, June 11-15, Boston, Massachusetts, 2000.

[9] D. K. Tafti, GenIDLEST - A Scalable Parallel Computational Tool for Simulating Complex Turbulent Flows, ASME-IMECE, FED -Vol. 256, Nov. 2001, New York.

[10] L.W. Zhang, S. Balachandar, and D.K. Tafti, Effect of intrinsic three dimensionality on heat transfer and friction loss in a periodic array of parallel plates, *Numerical Heat Transfer*, *Part A*, 31, pp. 327-353, 1997.

[11] L.W. Zhang, personal communication, Modine Manufacturing Company, 2000.

[12] M.S. Chong, A.E. Perry, and B.J. Cantwell, A general classification of three-dimensional flow fields, *Physics of Fluids A* 2(5), pp. 765-777, 1990.

[13] Y.-J. Chang. K.-C Hsu, Y.-T. Lin, C.-C. Wang, A generalized friction correlation for louver fin geometry, *Int. J. Heat Mass Transfer*, Vol. 43, pp. 2237-2243, 2000.

[14] Y.-J. Chang and C.-C. Wang, A generalized heat transfer correlation for louvered fin geometry, *Int. J. Heat Mass Transfer*, Vol. 40, No. 3, pp. 533-544, 1997.

[15] B. Sunden, J. Svantesson, Correlations of *j*- and *f*-factors for multilouvered heat transfer surfaces, in: proceedings of Third UK National Heat Transfer Conference, pp. 805-811, 1992.

Chapter 3. Modified Louvers

Two types of modified louver geometries were evaluated. The definition of the geometry is shown in Figure 3.1. For the first geometry, only a sweep angle (θ in Figure 3.1) of 15 and 30 degrees in the streamwise direction was introduced. In the second geometry, an additional angle was introduced along the fin height. For each geometry, flow and heat transfer at three nominal Reynolds numbers, Re=1,100, 600 and 300 are reported.

Figure 3.2 shows the heat transfer coefficient on the louver as well as the tube surface compared to a straight conventional louver. Modified louvers based on imposing a sweep angle to the leading and trailing edge of the louver were found to be ineffectual in increasing heat transfer.

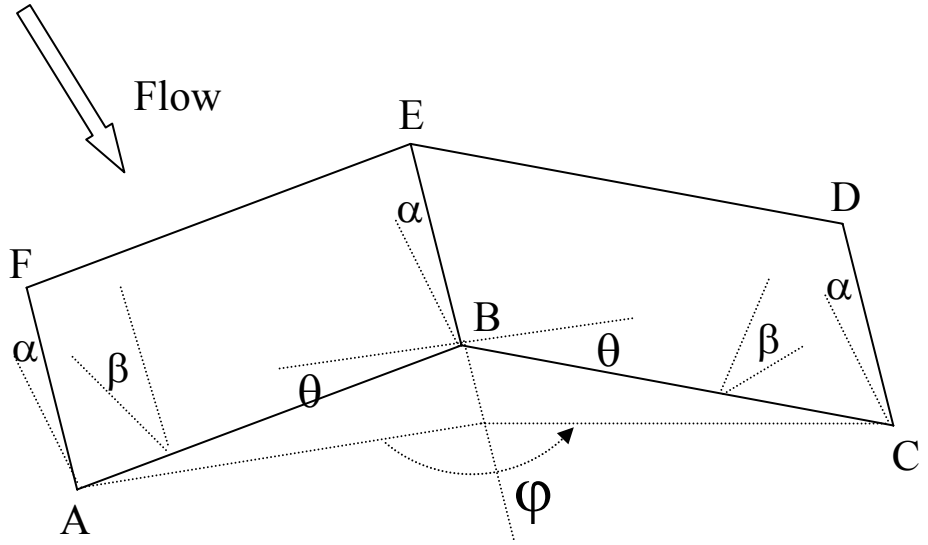

Figure 3.1. Definition of modified louver geometry. Schematic shows a single louver with line segments FA and CD lying on the tube surface. α is the angle between the flow direction and line LAF , LBE or LCD; θ is the sweep angle for LAB and LBC in the plane ABC; β is the angle between the plane ABC and plane ABEF (or BCDE); φ is the angle between the plane ABEF and BCDE, where ABEF and BCDE are two half louvers. Fin height is 5 louver pitches, same as the base louver.

Model 1:
(a) $\alpha = 25^o$ and $\theta = 15^o$, $\beta = 25^o$, $\varphi = 180^o$;
(b) $\alpha = 25^o$ and $\theta = 30^o$, $\beta = 25^o$, $\varphi = 180^o$;
Model 2:
(a) $\alpha = 25^o$ and $\theta = 15^o$, $\beta = 25.8^o$, $\varphi = 169.1^o$;
(b) $\alpha = 25^o$ and $\theta = 30^o$, $\beta = 28.3^o$, $\varphi = 152.8^o$.

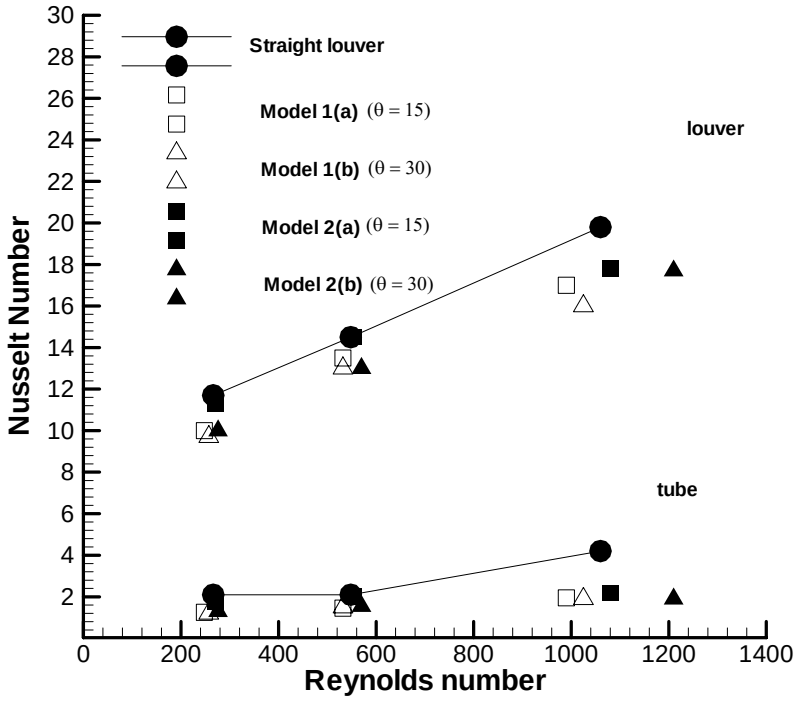

Figure 3.2: Nusselt number distribution for modified louvers compared to a straight unmodified louver.